

Investigating the Cytotoxicity of Ru(II) Polypyridyl Complexes by Changing the Electronic Structure of Salicylaldehyde Ligands

Maryam Taghizadeh Shool, Hadi Amiri Rudbari,* José V. Cuevas-Vicario,* Andrea Rodríguez-Rubio, Claudio Stagno, Nunzio Iraci, Thomas Efferth, Ejlal A. Omer, Tanja Schirmeister, Olivier Blacque, Nakisa Moini, Esmail Sheibani, and Nicola Micale*



Cite This: *Inorg. Chem.* 2024, 63, 1083–1101



Read Online

ACCESS |



Metrics & More

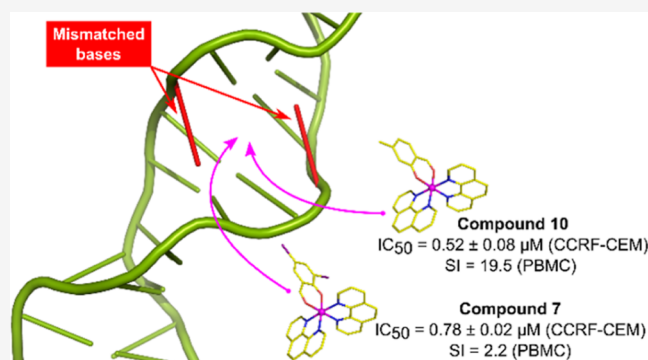


Article Recommendations



Supporting Information

ABSTRACT: A novel class of Ru(II)-based polypyridyl complexes with an auxiliary salicylaldehyde ligand $[\text{Ru}(\text{phen})_2(\text{X-Sal})]\text{BF}_4$ {X: H (1), 5-Cl (2), 5-Br (3), 3,5-Cl₂ (4), 3,5-Br₂ (5), 3-Br,5-Cl (6), 3,5-I₂ (7), 5-NO₂ (8), 5-Me (9), 4-Me (10), 4-OMe (11), and 4-DEA (12)}, has been synthesized and characterized by elemental analysis, FT-IR, and ¹H/¹³C NMR spectroscopy. The molecular structure of 4, 6, 9, 10, and 11 was determined by single-crystal X-ray diffraction analysis which revealed structural similarities. DFT and TD-DFT calculations showed that they also possess similar electronic structures. Absorption/emission spectra were recorded for 2, 3, 10, and 11. All Ru-complexes, unlike the pure ligands and the complex lacking the salicylaldehyde component, displayed outstanding antiproliferative activity in the screening test (10 μM) against CCRF-CEM leukemia cells underlining the crucial role of the presence of the auxiliary ligand for the biological activity. The two most active derivatives, namely 7 and 10, were selected for continuous assays showing IC₅₀ values in the submicromolar and micromolar range against drug-sensitive CCRF-CEM and multidrug-resistant CEM/ADR5000 leukemia cells, respectively. These two compounds were investigated in silico for their potential binding to duplex DNA well-matched and mismatched base pairs, since they showed remarkable selectivity indexes (2.2 and 19.5 respectively) on PBMC cells.



INTRODUCTION

Cancer still represents a leading cause of death globally. According to the WHO reports, it accounted for nearly 10 million deaths in the year 2020, or nearly one in six deaths.¹ However, if diagnosed and treated promptly, many types of cancer can be cured effectively.² The most common methods of cancer treatment include surgery, radiotherapy, chemotherapy, hormonal treatments, and targeted (small-molecule drugs or monoclonal antibodies) and biological therapies (which eventually affect the immune system). In this context, metal-based compounds have noticeable potential as chemotherapeutic agents,^{3,4} in particular platinum-based drugs (cisplatin and its best-known derivatives carboplatin and oxaliplatin) which still represent the most used metal-based chemotherapeutics for the treatment of various tumors. Although these drugs are very effective in killing cancer cells, they bring about many toxic side-effects and drug resistance phenomena,^{5–7} factors that have directed the pharmaceutical industry toward the search for alternative nonplatinum-based metal compounds as cytostatic agents.^{8,9}

In this regard, ruthenium-based complexes are considered as reasonable candidates for anticancer drug design as they have several advantages over platinum-based drugs including: (1)

several accessible and stable oxidation states under physiological conditions; (2) iron-mimicking ability in binding specific proteins which results in up-regulation of transferrin receptors on the cell surface and eventually in higher accumulation of ruthenium inside tumor cells compared to healthy cells; (3) various activation mechanisms combined with high biological activity; and (4) slow ligand exchange in vivo.^{10–12} As of yet, a number of ruthenium-based complexes, such as $[\text{RuCl}_4(\text{DMSO})(\text{Im})]\text{ImH}$; Im = imidazole) and $(\text{trans-}[\text{RuCl}_4(\text{Ind})_2]\text{IndH})$; Ind = indole) (known as NAMI-A and KP1019, respectively; Figure 1), have shown promising anticancer activity and completed phase I and II clinical studies, which spurred efforts to develop new Ru-based compounds for the treatment of cancer.^{13–15}

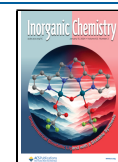
The oldest Ru(II)-based complexes endowed with polypyridyl ligands and whose biological activity has been investigated,

Received: September 30, 2023

Revised: December 11, 2023

Accepted: December 18, 2023

Published: December 29, 2023



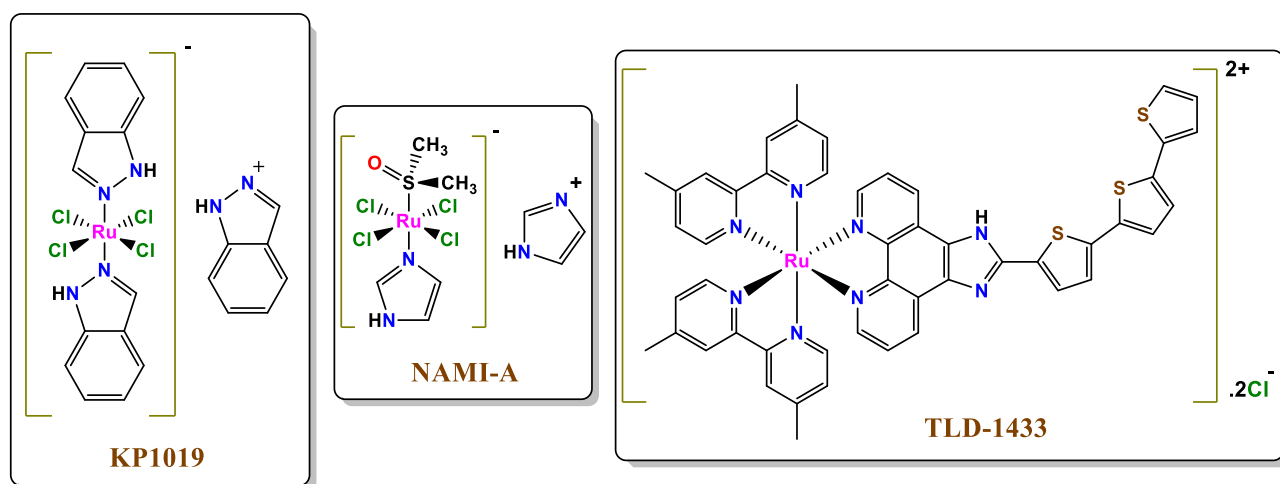


Figure 1. Chemical structure of KP1019, NAMI-A, and TLD-1433.

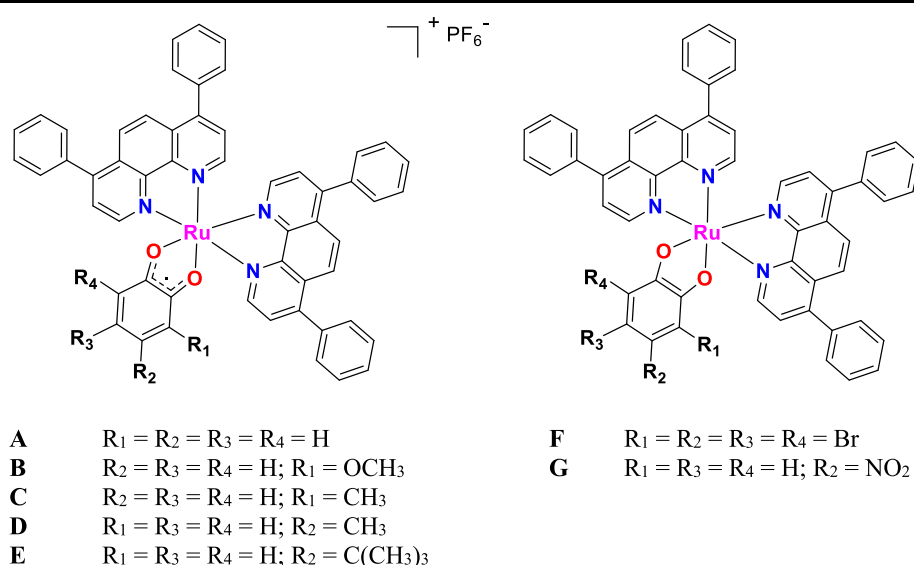


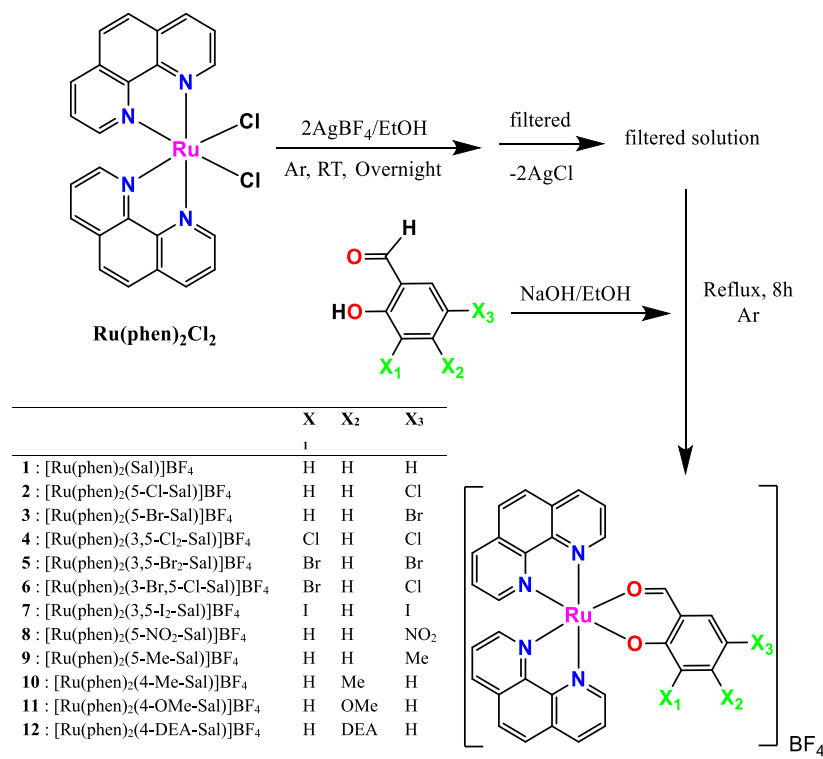
Figure 2. Chemical structure of the complexes $[Ru(DIP)_2(sq)](PF_6)$ developed by Notaro et al.²⁰

namely $[Ru(bpy)_3](ClO_4)_2$ and $[Ru(phen)_3](ClO_4)_2$, date back to the 1950s.¹⁶ Since then, polypyridyl ligands with multiple covalently bonded pyridine groups have been extensively used in medicinal inorganic chemistry due to their unique photochemical, physicochemical, and biological properties.¹⁷ The most important of the Ru(II)-based polypyridyl complexes developed so far is considered the photosensitizer TLD-1433 which has completed phase I and II clinical trials for photodynamic therapy treatment of the nonmuscle invasive bladder cancer (Figure 1).^{18,19}

On the basis of previous studies, it has been determined that the chemical/electronic characteristics and position of the substituents in the structure of the ligand play a crucial role in the cytotoxic behavior of this type of complexes. To get insights into their structure–activity relationships, Notaro et al. have recently studied Ru(II) polypyridyl complexes with substituted catecholate ligands bearing either electron-donating (EDG) or electron-withdrawing groups (EWG), namely $[Ru(DIP)_2(sq)](PF_6)$ (Figure 2).²⁰ As indicated in this work, the difference in electron density on the catecholate ligand induces a variation in its oxidation state when coordinating with the metal center. The

variation of the oxidation state of the ligand affects the physicochemical properties and biological activity of the resulting complexes. The cytotoxicity data revealed that the complexes with ligands bearing EDG show much higher bioactivity as compared to complexes with ligands bearing EWG as a substitution pattern. The complex with—OMe substitution (i.e., **B**; Figure 2) turned out to be the most promising compound of this series.²⁰

In 2020, we have successfully synthesized a set of copper(II)-based complexes with general formula $Cu(\text{diimine})(x\text{-Sal})(NO_3)$ and investigated the effects of various halogen atoms on the diimine ligand and their impact on the antiproliferative activity against two different cancer cell lines.²¹ The obtained results highlighted that the bpy derivatives are valid candidates for further in vitro and in vivo studies. We also synthesized a new set of chiral Ru(II) polypyridyl complexes, namely $\Delta/\Lambda-[Ru(bpy)_2(X,Y\text{-Sal})]BF_4$, where X,Y-Sal is halogenated salicylaldehyde with chloride and/or bromide substitutions in 3 and 5 positions.²² We also found that the type, number, and position of the halogen substituents are important factors in determining the cytotoxicity of these compounds.

Scheme 1. Synthetic Route and Chemical Structure of the Newly Synthesized Ru(II) Complexes $[\text{Ru}(\text{phen})_2(\text{X-Sal})]\text{BF}_4$ (1–12)

Herein, we report synthesis, structural characterization, photophysical properties, antiproliferative activity, SAR analysis of the ligand substitution pattern, and computational study on the expected biomolecular target (i.e., DNA) of a new set of 12 Ru(II) polypyridyl complexes obtained from the starting complex $\text{Ru}(\text{phen})_2\text{Cl}_2$ and substituted salicylaldehyde ligands (Scheme 1).

EXPERIMENTAL SECTION

Chemicals and Instrumentation. Ruthenium(III)-chloride hydrate, 1,10-phenanthroline, sodium hydroxide, silver tetrafluoroborate, salicylaldehyde, 5-chlorosalicylaldehyde, 3,5-chlorosalicylaldehyde, 5-bromosalicylaldehyde, 3,5-bromosalicylaldehyde, 3-bromo-5-chlorosalicylaldehyde, 3,5-diiodosalicylaldehyde, 4-(diethylamino)salicylaldehyde, 5-nitrosalicylaldehyde, 4-methoxysalicylaldehyde, 5-methoxysalicylaldehyde, 4-methylsalicylaldehyde, 5-methylsalicylaldehyde were obtained from Sigma-Aldrich and used without any further purification. The solvents obtained from the same commercial source, however, were subjected to a distillation process before being used for the synthesis of the complexes. *cis*- $\text{Ru}(\text{phen})_2\text{Cl}_2$ was prepared according to literature procedures.²³ FT-IR spectra were recorded using KBr pellets on a JASCO FT/IR-6300 spectrometer (4000–400 cm^{-1}). Elemental analyses were carried out using both the LECO's CHNS-932 and PerkinElmer 7300 DV elemental analyzer. NMR spectra were recorded in quartz NMR tube by means of Bruker high resolution Avance NEO 4500 (500 MHz) and Bruker Avance III HD 400 MHz spectrometer and using DMSO- d_6 as a solvent at 295 K.

Synthesis of the Complexes. All $[\text{Ru}(\text{phen})_2\text{L}]\text{BF}_4$ complexes were obtained by a general synthetic method. Briefly, the starting complex $\text{Ru}(\text{phen})_2\text{Cl}_2$ (1 mmol) and AgBF_4 (2 mmol) were dissolved in ethanol. The resulting reaction solution was then stirred overnight at room temperature and under argon atmosphere. After that, the reaction mixture was filtered to remove the AgCl that had formed in the meantime and to the resulting orange-red solution were added in sequence an ethanol solution of substituted salicylaldehyde (HL) (1 mmol) and NaOH (1 mmol). The new reaction mixture was stirred at reflux and under argon atmosphere for ~8 h. The solvent was then

removed under vacuum providing a solid which was dissolved in the minimum amount of chloroform and precipitated with *n*-hexane.

$[\text{Ru}(\text{phen})_2(\text{Sal})]\text{BF}_4$ (1). Yield 89%. Anal. Calcd for $\text{C}_{31}\text{H}_{21}\text{BF}_4\text{N}_4\text{O}_2\text{Ru}$: C, 55.62; H, 3.16; N, 8.37. Found: C, 55.65; H, 3.15; N, 8.39. IR (KBr, cm^{-1}): 1605 (s, C=O), 1057 (s, B–F). ^1H NMR (400 MHz, DMSO- d_6): δ ppm 9.19 (dd, 1H, H⁶ or H²¹), 9.17 (s, 1H, H¹), 9.10 (dd, 1H, H⁶ or H²¹), 8.87 (dd, 1H, H⁸ or H¹⁹), 8.83 (dd, 1H, H⁸ or H¹⁹), 8.49 (m, 2H, H¹¹ and H¹⁶), 8.38 (d, 2H, H⁹ and H¹⁸), 8.29 (m, 2H, H¹⁰ and H¹⁷), 8.18 (dd, 1H, H⁷ or H²⁰ or H¹³ or H¹⁴), 8.11 (m, 2H, H⁷ or H²⁰ or H¹³ or H¹⁴), 8.04 (d, 1H, H⁷ or H²⁰ or H¹³ or H¹⁴), 7.52 (td, 2H, H¹², H¹⁵), 7.42 (dd, 1H, H²), 7.20 (m, 1H, H³ or H⁴), 6.52 (d, 1H, H⁵), 6.44 (t, 1H, H³ or H⁴). ^{13}C NMR (100 MHz, DMSO- d_6): δ ppm 190.1 (C¹), 170.3 (C²³), 154.7 (C¹³ or C¹⁴), 154.3 (C¹³ or C¹⁴), 151.1 (C⁶ or C²¹), 151.0 (C⁶ or C²¹), 149.9 (C²⁷ or C²⁸), 149.3 (C²⁷ or C²⁸), 148.3 (C²⁴ or C³¹), 148.1 (C²⁴ or C³¹), 137.3 (C² or C⁵), 136.1 (C² or C⁵), 136.0 (C⁸ or C¹⁹), 135.6 (C⁸ or C¹⁹), 134.3 (C¹¹ or C¹⁶), 134.1 (C¹¹ or C¹⁶), 130.0, 129.9, 129.9, and 129.7 (C²⁵, C²⁶, C²⁹ and C³⁰), 127.7, 127.6 (C⁹, C¹⁰, C¹⁷ and C¹⁸), 125.8 (C⁷ or C²⁰), 125.5 (C⁷ or C²⁰), 124.8 (C¹² or C¹⁵), 124.7 (C¹² or C¹⁵), 124.2 (C²²), 122.2 (C³ or C⁴), 114.2 (C³ or C⁴).

$[\text{Ru}(\text{phen})_2(5\text{-Cl-Sal})]\text{BF}_4$ (2). Yield 84%. Anal. Calcd for $\text{C}_{31}\text{H}_{20}\text{BClF}_4\text{N}_4\text{O}_2\text{Ru}$: C, 52.90; H, 2.86; N, 7.96. Found: C, 52.94; H, 2.89; N, 7.97. IR (KBr, cm^{-1}): 1580 (s, C=O), 1058 (s, B–F). ^1H NMR (500 MHz, DMSO- d_6): δ ppm 9.21–9.17 (m, 2H, H¹ and H⁵), 9.08 (dd, $J = 5.1, 1.3$ Hz, 1H, H²⁰), 8.88 (dd, $J = 8.3, 1.3$ Hz, 1H, H¹⁸), 8.83 (dd, $J = 8.2, 1.3$ Hz, 1H, H⁷), 8.50 (dd, $J = 8.2, 1.2$ Hz, 1H, H¹⁰ or H¹⁵), 8.47 (dd, $J = 8.2, 1.2$ Hz, 1H, H¹⁰ or H¹⁵), 8.38 (m, 1.8 Hz, 2H, H⁸ and H¹⁷), 8.29 (d, $J = 6.3$ Hz, 1H, H⁹ or H¹⁶), 8.27 (d, $J = 6.2$ Hz, 1H, H⁹ or H¹⁶), 8.18 (dd, $J = 8.3, 5.1$ Hz, 1H, H¹⁹), 8.11 (dd, $J = 8.2, 5.2$ Hz, 1H, H⁶), 8.08 (dd, $J = 5.4, 1.2$ Hz, 1H, H¹² or H¹³), 8.02 (dd, $J = 5.3, 1.2$ Hz, 1H, H¹² or H¹³), 7.55–7.48 (m, 3H, H² and H¹¹ and H¹⁴), 7.17 (dd, $J = 9.4, 2.9$ Hz, 1H, H⁴), 6.53 (d, $J = 9.4$ Hz, 1H, H³). ^{13}C NMR (126 MHz, DMSO- d_6): δ ppm 189.7 (C¹), 168.9 (C²³), 154.8 (C¹² or C¹³), 154.4 (C¹² or C¹³), 151.3 (C⁵ or C²⁰), 151.1 (C⁵ or C²⁰), 149.8 (C²⁷ or C²⁸), 149.3 (C²⁷ or C²⁸), 148.3 (C²⁴ or C³¹), 148.1 (C²⁴ or C³¹), 136.3 (C⁷ or C¹⁸), 135.9 (C⁷ or C¹⁸), 135.5 (C⁴), 134.8 (C²), 134.5 (C¹⁰ or C¹⁵), 134.3 (C¹⁰ or C¹⁵), 130.1, 130.0, 129.9, and 129.7 (C²⁵, C²⁶, C²⁹ and C³⁰), 127.7 and 127.6 (C⁸, C⁹, C¹⁶ and C¹⁷), 126.8 (C³), 125.9 (C⁶ or

(C¹⁹), 125.6 (C⁶ or C¹⁹), 124.9 (C¹¹ or C¹⁴), 124.7 (C¹¹ or C¹⁴), 122.8 (C²¹), 117.1 (C²²).

[Ru(phen)₂(5-Br-Sal)]BF₄ (3). Yield 81%. Anal. Calcd for C₃₁H₂₀BBrF₄N₄O₂Ru: C, 49.76; H, 2.69; N, 7.49. Found: C, 49.78; H, 2.72; N, 7.53. IR (KBr, cm⁻¹): 1648 (s, C=O), 1060 (s, B-F). ¹H NMR (500 MHz, DMSO-*d*₆): δ ppm 9.18 (m, 2H, H¹ and H⁵), 9.08 (dd, *J* = 5.1, 1.3 Hz, 1H, H²⁰), 8.88 (dd, *J* = 8.3, 1.3 Hz, 1H, H¹⁸), 8.83 (dd, *J* = 8.2, 1.2 Hz, 1H, H⁷), 8.50 (dd, *J* = 8.2, 1.1 Hz, 1H, H¹⁰ or H¹⁵), 8.47 (dd, *J* = 8.2, 1.1 Hz, 1H, H⁸ or H¹⁵), 8.38 (m, 2H, H⁸ and H¹⁷), 8.27 (m, 2H, H⁹ and H¹⁶), 8.18 (dd, *J* = 8.3, 5.1 Hz, 1H, H¹⁹), 8.11 (dd, *J* = 8.2, 5.2 Hz, 1H, H⁶), 8.08 (dd, *J* = 5.3, 1.1 Hz, 1H, H¹² or H¹³), 8.02 (dd, *J* = 5.4, 1.1 Hz, 1H, H¹² or H¹³), 7.65 (d, *J* = 2.8 Hz, 1H, H²), 7.51 (m, 2H, H¹¹ and H¹⁴), 7.24 (dd, *J* = 9.4, 2.8 Hz, 1H, H⁴), 6.47 (d, *J* = 9.4 Hz, 1H, H³). ¹³C NMR (126 MHz, DMSO-*d*₆): δ ppm 189.7 (C¹), 169.1 (C²³), 154.8 (C¹² or C¹³), 154.4 (C¹² or C¹³), 151.3 (C⁵ or C²⁰), 151.1 (C⁵ or C²⁰), 149.8 (C²⁷ or C²⁸), 149.3 (C²⁷ or C²⁸), 148.3 (C²⁴ or C³¹), 148.1 (C²⁴ or C³¹), 138.1 (C² or C⁴), 137.9 (C² or C⁴), 136.4 (C⁷ or C¹⁸), 135.9 (C⁷ or C¹⁸), 134.5 (C¹⁰ or C¹⁵), 134.3 (C¹⁰ or C¹⁵), 130.1, 130.0, 129.9 and 129.8 (C²⁵, C²⁶, C²⁹ and C³⁰), 127.7 and 127.6 (C⁸, C⁹, C¹⁶ and C¹⁷), 127.1 (C³), 125.9 (C⁶ or C¹⁹), 125.6 (C⁶ or C¹⁹), 124.9 (C¹¹ or C¹⁴), 124.7 (C¹¹ or C¹⁴), 123.8 (C²¹), 104.1 (C²²).

[Ru(phen)₂(3,5-Cl₂-Sal)]BF₄ (4). Yield 85%. Anal. Calcd for C₃₁H₉BCl₂F₄N₄O₂Ru: C, 50.43; H, 2.59; N, 7.59. Found: C, 50.46; H, 2.61; N, 7.60. IR (KBr, cm⁻¹): 1592 (s, C=O), 1061 (s, B-F). ¹H NMR (400 MHz, DMSO-*d*₆): δ ppm 9.33 (s, 1H, H¹), 9.22 (dd, 1H, H⁴ or H¹⁹), 9.00 (dd, 1H, H⁴ or H¹⁹), 8.91 (dd, 1H, H¹⁷ or H⁶), 8.86 (dd, 1H, H¹⁷ or H⁶), 8.51 (t, 2H, H⁵ and H¹⁸), 8.39 (m, 2H, H¹⁴ and H⁹), 8.29 (m, 2H, H⁷ and H¹⁶ or H⁸ and H¹⁵ or H¹¹ and H¹²), 8.21 (dd, 1H, H⁷ and H¹⁶ or H⁸ and H¹⁵ or H¹¹ and H¹²), 8.12 (m, 2H, H⁷ and H¹⁶ or H⁸ and H¹⁵ or H¹¹ and H¹²), 8.06 (dd, 1H, H⁷ and H¹⁶ or H⁸ and H¹⁵ or H¹¹ and H¹²), 7.58 (dd, 2H, H² and H³), 7.54 (dd, 2H, H¹⁰ and H¹³). ¹³C NMR (100 MHz, DMSO-*d*₆): δ ppm 190.9 (C¹), 162.3 (C²³), 155.0 (C¹¹ or C¹²), 154.4 (C¹¹ or C¹²), 151.3 (C⁴ or C¹⁹), 150.8 (C⁴ or C¹⁹), 149.8 (C²⁷ or C²⁸), 149.2 (C²⁷ or C²⁸), 148.2 (C²⁴ or C³¹), 148.0 (C²⁴ or C³¹), 136.5 (C⁶ or C¹⁷), 136.1 (C⁶ or C¹⁷), 136.6 (C² or C³), 134.5 (C² or C³), 134.3 (C⁹ or C¹⁴), 133.8 (C⁹ or C¹⁴), 130.0, 130.0, 129.9, and 129.6 (C²⁵, C²⁶, C²⁹ and C³⁰), 129.1 (C²¹ or C²²), 127.7 and 126.6 (C⁷, C⁸, C¹⁵ and C¹⁶), 126.1 (C⁵ or C¹⁸), 125.6 (C⁵ or C¹⁸), 124.9 (C¹⁰ or C¹³), 124.7 (C¹⁰ or C¹³), 123.0 (C²⁰), 116.0 (C²¹ or C²²).

[Ru(phen)₂(3,5-Br₂-Sal)]BF₄ (5). Yield 92%. Anal. Calcd for C₃₁H₉BBr₂F₄N₄O₂Ru: C, 45.01; H, 2.32; N, 6.77. Found: C, 45.04; H, 2.30; N, 6.79. IR (KBr, cm⁻¹): 1586 (s, C=O), 1059 (s, B-F). ¹H NMR (400 MHz, DMSO-*d*₆): δ ppm 9.33 (s, 1H, H¹), 9.22 (dd, 1H, H⁴ or H¹⁹), 8.98 (dd, 1H, H⁴ or H¹⁹), 8.91 (dd, 1H, H¹⁷ or H⁶), 8.85 (dd, 1H, H¹⁷ or H⁶), 8.50 (m, 2H, H⁹ and H¹⁴), 8.39 (t, 2H, H¹⁸ and H⁵), 8.29 (m, 2H, H⁷ and H¹⁶ or H⁸ and H¹⁵ or H¹¹ and H¹²), 8.23 (dd, 1H, H⁷ and H¹⁶ or H⁸ and H¹⁵ or H¹¹ and H¹²), 8.13 (m, 2H, H⁷ and H¹⁶ or H⁸ and H¹⁵ or H¹¹ and H¹²), 8.07 (dd, 1H, H⁷ and H¹⁶ or H⁸ and H¹⁵ or H¹¹ and H¹²), 7.76 (dd, 2H, H² and H³), 7.54 (dd, 2H, H¹⁰ and H¹³). ¹³C NMR (100 MHz, DMSO-*d*₆): δ ppm 191.0 (C¹), 162.9 (C²³), 155.0 (C¹¹ or C¹²), 154.4 (C¹¹ or C¹²), 151.3 (C⁴ or C¹⁹), 150.8 (C⁴ or C¹⁹), 149.8 (C²⁷ or C²⁸), 149.2 (C²⁷ or C²⁸), 148.2 (C²⁴ or C³¹), 148.0 (C²⁴ or C³¹), 139.0 (C² or C³), 138.3 (C² or C³), 136.5 (C⁶ or C¹⁷), 136.1 (C⁶ or C¹⁷), 134.6 (C⁹ or C¹⁴), 134.5 (C⁹ or C¹⁴), 130.0, 129.9, and 129.6 (C²⁵, C²⁶, C²⁹ and C³⁰), 127.7, 127.6, and 127.6 (C⁷, C⁸, C¹⁵ and C¹⁶), 126.1 (C⁵ or C¹⁸), 125.6 (C⁵ or C¹⁸), 124.9 (C¹⁰ or C¹³), 124.6 (C¹⁰ or C¹³), 123.5 (C²⁰), 120.6 (C²¹ or C²²), 103.2 (C²¹ or C²²).

[Ru(phen)₂(3-Br-5Cl-Sal)]BF₄ (6). Yield 80%. Anal. Calcd for C₃₁H₉BBrClF₄N₄O₂Ru: C, 47.57; H, 2.45; N, 8.05. Found: C, 47.60; H, 2.46; N, 8.08. IR (KBr, cm⁻¹): 1586 (s, C=O), 1061 (s, B-F). ¹H NMR (400 MHz, DMSO-*d*₆): δ ppm 9.33 (s, 1H, H¹), 9.21 (dd, 1H, H⁴ or H¹⁹), 8.98 (dd, 1H, H⁴ or H¹⁹), 8.90 (dd, 1H, H¹⁷ or H⁶), 8.85 (dd, 1H, H¹⁷ or H⁶), 8.50 (m, 2H, H⁹ and H¹⁴), 8.39 (t, 2H, H¹⁸ and H⁵), 8.30 (m, 2H, H⁷ and H¹⁶ or H⁸ and H¹⁵ or H¹¹ and H¹²), 8.23 (dd, 1H, H⁷ and H¹⁶ or H⁸ and H¹⁵ or H¹¹ and H¹²), 8.13 (m, 2H, H⁷ and H¹⁶ or H⁸ and H¹⁵ or H¹¹ and H¹²), 8.06 (dd, 1H, H⁷ and H¹⁶ or H⁸ and H¹⁵ or H¹¹ and H¹²), 7.70 (dd, 2H, H² or H³), 7.63 (dd, 2H, H² or H³), 7.54 (dd, 2H, H¹⁰ and H¹³). ¹³C NMR (100 MHz, DMSO-*d*₆): δ ppm 191.0 (C¹), 162.8 (C²³), 155.0 (C¹¹ or C¹²), 154.4 (C¹¹ or C¹²), 151.3 (C⁴ or C¹⁹), 150.8 (C⁴ or C¹⁹), 149.8 (C²⁷ or C²⁸), 149.2 (C²⁷ or C²⁸), 148.2

(C²⁴ or C³¹), 148.0 (C²⁴ or C³¹), 136.8 (C² or C³), 136.5 (C² or C³), 136.1 (C⁶ or C¹⁷), 135.0 (C⁶ or C¹⁷), 134.6 (C⁹ or C¹⁴), 134.5 (C⁹ or C¹⁴), 130.0, 129.9, and 129.58 (C²⁵, C²⁶, C²⁹ and C³⁰), 127.7, 127.6, and 127.6 (C⁷, C⁸, C¹⁵ and C¹⁶), 126.1 (C⁵ or C¹⁸), 125.6 (C⁵ or C¹⁸), 124.9 (C¹⁰ or C¹³), 124.6 (C¹⁰ or C¹³), 122.4 (C²⁰), 120.3 (C²¹ or C²²), 116.6 (C²¹ or C²²).

[Ru(phen)₂(3,5-I₂-Sal)]BF₄ (7). Yield 94%. Anal. Calcd for C₃₁H₉BF₄I₂N₄O₂Ru: C, 40.42; H, 2.08; N, 6.08. Found: C, 40.47; H, 2.11; N, 6.09. IR (KBr, cm⁻¹): 1568 (s, C=O), 1073 (s, B-F). ¹H NMR (400 MHz, DMSO-*d*₆): δ ppm 9.26 (s, 1H, H¹), 9.19 (dd, 1H, H⁴ or H¹⁹), 8.94 (dd, 1H, H⁴ or H¹⁹), 8.91 (dd, 1H, H¹⁷ or H⁶), 8.84 (dd, 1H, H¹⁷ or H⁶), 8.51 (m, 2H, H⁹ and H¹⁴), 8.39 (m, 2H, H¹⁸ and H⁵), 8.29 (m, 2H, H⁷ and H¹⁶ or H⁸ and H¹⁵ or H¹¹ and H¹²), 8.23 (m, 2H, H⁷ and H¹⁶ or H⁸ and H¹⁵ or H¹¹ and H¹²), 8.09 (m, 2H, H⁷ and H¹⁶ or H⁸ and H¹⁵ or H¹¹ and H¹²), 7.95 (dd, 1H, H² or H³), 7.85 (dd, 1H, H² or H³), 7.54 (m, 2H, H¹⁰ and H¹³). ¹³C NMR (100 MHz, DMSO-*d*₆): δ ppm 191.0 (C¹), 164.9 (C²³), 155.0 (C¹¹ or C¹²), 154.4 (C¹¹ or C¹²), 151.3 (C⁴ or C¹⁹), 150.8 (C⁴ or C¹⁹), 149.8 (C²⁷ or C²⁸), 149.5 (C²⁷ or C²⁸), 149.4 (C² or C³), 148.2 (C²⁴ or C³¹), 148.1 (C²⁴ or C³¹), 145.5 (C² or C³), 136.5 (C⁶ or C¹⁷), 136.0 (C⁶ or C¹⁷), 134.5 (C⁹ or C¹⁴), 134.39 (C⁹ or C¹⁴), 130.0, 129.9, 129.9 and 129.5 (C²⁵, C²⁶, C²⁹ and C³⁰), 127.7, 127.6, 127.6 and 127.56 (C⁷, C⁸, C¹⁵ and C¹⁶), 126.1 (C⁵ or C¹⁸), 125.5 (C⁵ or C¹⁸), 125.0 (C¹⁰ or C¹³), 124.5 (C¹⁰ or C¹³), 123.1 (C²⁰), 100.4 (C²¹ or C²²) 74.0 (C²¹ or C²²).

[Ru(phen)₂(5-NO₂-Sal)]BF₄ (8). Yield 87%. Anal. Calcd for C₃₁H₂₀BF₄N₅O₄Ru: C, 52.12; H, 2.28; N, 9.80. Found: C, 52.13; H, 2.30; N, 9.84. IR (KBr, cm⁻¹): 1594 (s, C=O), 1062 (s, B-F). ¹H NMR (400 MHz, DMSO-*d*₆): δ ppm 9.52 (s, 1H, H¹), 9.24 (d, 1H, H⁵ or H²⁰), 9.08 (d, 1H, H⁵ or H²⁰), 8.91 (d, 1H, H⁷ or H¹⁸), 8.87 (d, 1H, H⁷ or H¹⁸), 8.66 (d, 1H, H²), 8.51 (t, 2H, H¹⁰ and H¹⁵), 8.39 (dd, 2H, H⁶ and H¹⁹), 8.31 (m, 2H, H⁸ and H¹⁷ or H⁹ and H¹⁶ or H¹² or H¹³), 8.19 (m, 1H, H⁸ and H¹⁷ or H⁹ and H¹⁶ or H¹² or H¹³), 8.12 (m, 2H, H⁸ and H¹⁷ or H⁹ and H¹⁶ or H¹² or H¹³), 8.05 (d, 1H, H⁸ and H¹⁷ or H⁹ and H¹⁶ or H¹² or H¹³), 7.92 (dd, 1H, H⁴), 7.53 (dt, 2H, H¹¹ and H¹⁴), 6.60 (d, 1H, H³). ¹³C NMR (100 MHz, DMSO-*d*₆): δ ppm 190.3 (C¹), 170.1 (C²³), 153.5 (C¹² or C¹³), 153.2 (C¹² or C¹³), 151.1 (C⁵ or C²⁰), 150.9 (C⁵ or C²⁰), 149.3 (C²⁷ or C²⁸), 148.8 (C²⁷ or C²⁸), 147.7 (C²⁴ or C³¹), 147.2 (C²⁴ or C³¹), 139.6 (C⁷ or C¹⁸), 139.1 (C⁷ or C¹⁸), 136.9 (C⁴), 135.2 (C²), 134.0 (C¹⁰ or C¹⁵), 133.7 (C¹⁰ or C¹⁵), 131.0, 130.9, 130.8, and 130.7 (C²⁵, C²⁶, C²⁹ and C³⁰), 127.9, 127.6, and 127.2 (C⁸, C⁹, C¹⁶ and C¹⁷), 126.1 (C³), 125.9 (C⁶ or C¹⁹), 125.5 (C⁶ or C¹⁹), 124.7 (C¹¹ or C¹⁴), 124.2 (C¹¹ or C¹⁴), 123.0 (C²¹), 116.3 (C²²).

[Ru(phen)₂(5-Me-Sal)]BF₄ (9). Yield 84%. Anal. Calcd For C₃₂H₂₃BF₄N₄O₂Ru: C, 56.24; H, 3.39; N, 8.20. Found: C, 56.29; H, 3.42; N, 8.24. IR (KBr, cm⁻¹): 1618 (s, C=O), 1058 (s, B-F). ¹H NMR (400 MHz, DMSO-*d*₆): δ ppm 9.16 (dd, 1H, H²⁰), 9.07 (m, 2H, H¹ and H⁵), 8.85 (dd, 1H, H¹⁸), 8.81 (dd, 1H, H¹⁸), 8.48 (dd, 1H, H¹⁰ or H¹⁵), 8.45 (dd, 1H, H¹⁰ or H¹⁵), 8.37 (m, 2H, H⁸ and H¹⁷), 8.27 (dd, 2H, H⁹ and H¹⁶), 8.16 (dd, 1H, H⁶), 8.09 (m, 2H, H¹⁹ and H¹² or H¹³), 8.02 (dd, 1H, H¹² or H¹³), 7.51 (td, 2H, H¹¹ and H¹⁴), 7.15 (d, 1H, H²), 7.03 (dd, 1H, H⁴), 6.44 (d, 1H, H³), 2.10 (s, 3H, Me). ¹³C NMR (126 MHz, DMSO-*d*₆): δ ppm 187.8 (C¹), 170.8 (C²³), 153.9 (C¹² or C¹³), 153.4 (C¹² or C¹³), 151.1 (C⁵ or C²⁰), 149.8 (C⁵ or C²⁰), 149.4 (C²⁷ or C²⁸), 149.1 (C²⁷ or C²⁸), 148.4 (C²⁴ or C³¹), 148.1 (C²⁴ or C³¹), 147.2 (C²²), 137.2 (C²), 136.2 (C⁷ or C¹⁸), 135.8 (C⁷ or C¹⁸), 133.8 (C¹⁰ or C¹⁵), 133.20 (C¹⁰ or C¹⁵), 130.2, 130.1, 129.9, and 129.8 (C²⁵, C²⁶, C²⁹ and C³⁰), 128.1, 127.9, and 127.9 (C⁸, C⁹, C¹⁶ and C¹⁷), 125.3 (C⁶ or C¹⁹), 125.0 (C⁶ or C¹⁹), 124.9 (C¹¹ or C¹⁴), 124.4 (C¹¹ or C¹⁴), 124.0 (C⁴), 119.3 (C²¹), 114.7 (C³), 21.0 (Me).

[Ru(phen)₂(4-Me-Sal)]BF₄ (10). Yield 84%. Anal. Calcd For C₃₂H₂₃BF₄N₄O₂Ru: C, 56.24; H, 3.39; N, 8.20. Found: C, 56.27; H, 3.41; N, 8.23. IR (KBr, cm⁻¹): 1622 (s, C=O), 1058 (s, B-F). ¹H NMR (500 MHz, DMSO-*d*₆): δ ppm 9.16 (dd, *J* = 5.2, 1.2 Hz, 1H, H²⁰), 9.09 (dd, *J* = 5.1, 1.3 Hz, 1H, H⁵), 9.03 (s, 1H, H¹), 8.85 (dd, *J* = 8.3, 1.3 Hz, 1H, H⁷), 8.81 (dd, *J* = 8.2, 1.2 Hz, 1H, H¹⁸), 8.48 (dd, *J* = 8.3, 1.2 Hz, 1H, H¹⁰ or H¹⁵), 8.46 (dd, *J* = 8.2, 1.2 Hz, 1H, H¹⁰ or H¹⁵), 8.37 (d, *J* = 8.9 Hz, 2H, H⁸ and H¹⁷), 8.28 (d, *J* = 3.3 Hz, 1H, H⁹ or H¹⁶), 8.26 (d, *J* = 3.3 Hz, 1H, H⁹ or H¹⁶), 8.17 (dd, *J* = 8.2, 5.1 Hz, 1H, H⁶), 8.12–8.07 (m, 2H, H¹⁹ and H¹² or H¹³), 8.02 (dd, *J* = 5.4, 1.2 Hz, 1H, H¹² or H¹³), 7.51 (td, *J* = 8.1, 5.3 Hz, 2H, H¹¹ and H¹⁴), 7.28 (d, *J* = 8.3 Hz, 1H, H²),

6.35 (s, 1H, H⁴), 6.28 (dd, *J* = 8.3, 1.5 Hz, 1H, H³), 1.99 (d, *J* = 0.8 Hz, 3H, Me). ¹³C NMR (126 MHz, DMSO-*d*₆): δ ppm 188.8 (C¹), 170.3 (C²³), 154.6 (C¹² or C¹³), 154.2 (C¹² or C¹³), 151.3 (C⁵ or C²⁰), 151.1 (C⁵ or C²⁰), 149.9 (C²⁷ or C²⁸), 149.4 (C²⁷ or C²⁸), 148.4 (C³¹), 148.2 (C²⁵), 147.0 (C²²), 137.0 (C²), 136.0 (C⁷), 135.5 (C¹⁸), 134.2 (C¹⁰ or C¹⁵), 134.0 (C¹⁰ or C¹⁵), 130.0, 129.9, 129.9, and 129.7 (C²⁴, C²⁶, C²⁹ and C³⁰), 127.7, 127.6, and 127.6 (C⁸, C⁹, C¹⁶ and C¹⁷), 125.8 (C⁶), 125.5 (C¹⁹), 124.8 (C¹¹ or C¹⁴), 124.6 (C¹¹ or C¹⁴), 123.8 (C⁴), 120.2 (C²¹), 116.5 (C³), 21.4 (Me).

[Ru(phen)₂(4-OMe-Sal)]BF₄ (**11**). Yield 90%. Anal. Calcd For C₃₂H₂₃BF₄N₄O₃Ru: C, 54.95; H, 3.31; N, 8.01. Found: C, 54.93; H, 3.34; N, 8.05. IR (KBr, cm⁻¹): 1612 (s, C=O), 1058 (s, B–F). ¹H NMR (500 MHz, DMSO-*d*₆): δ ppm 9.18 (dd, *J* = 5.2, 1.2 Hz, 1H, H²⁰), 9.12 (dd, *J* = 5.2, 1.3 Hz, 1H, H⁵), 8.88 (s, 1H, H¹), 8.84 (dd, *J* = 8.4, 1.3 Hz, 1H, H⁷), 8.82 (dd, *J* = 8.2, 1.2 Hz, 1H, H¹⁸), 8.46 (ddd, *J* = 8.2, 5.7, 1.2 Hz, 2H, H¹⁰ and H¹⁵), 8.38 (d, *J* = 6.1 Hz, 1H, H⁸ or H¹⁷), 8.36 (d, *J* = 6.0 Hz, 1H, H⁸ or H¹⁷), 8.28 (d, *J* = 2.2 Hz, 1H, H⁹ or H¹⁶), 8.26 (d, *J* = 2.2 Hz, 1H, H⁹ or H¹⁶), 8.18 (dd, *J* = 8.2, 5.2 Hz, 1H, H⁶), 8.12 (dd, *J* = 8.2, 5.2 Hz, 1H, H¹⁹), 8.04 (ddd, *J* = 7.6, 5.4, 1.2 Hz, 2H, H¹² and H¹³), 7.51 (ddd, *J* = 8.1, 5.4, 1.2 Hz, 2H, H¹¹ and H¹⁴), 7.27 (d, *J* = 9.1 Hz, 1H, H²), 6.10 (dd, *J* = 9.0, 2.4 Hz, 1H, H³), 6.02 (d, *J* = 2.4 Hz, 1H, H⁴), 3.60 (s, 3H, OMe). ¹³C NMR (126 MHz, DMSO-*d*₆): δ ppm 187.0 (C¹), 172.3 (C²³), 166.1 (C²²), 154.6 (C¹² or C¹³), 154.3 (C¹² or C¹³), 151.2 (C²⁰), 151.2 (C⁵), 150.0 (C²⁷ or C²⁸), 149.5 (C²⁷ or C²⁸), 148.4 (C²⁴ or C³¹), 148.3 (C²⁴ or C³¹), 138.5 (C²), 135.9 (C⁷ or C¹⁸), 135.5 (C⁷ or C¹⁸), 134.2 (C¹⁰ or C¹⁵), 134.0 (C¹⁰ or C¹⁵), 130.1, 130.0, 129.9, and 129.8 (C²⁵, C²⁶, C²⁹ and C³⁰), 127.7, 127.6, and 127.5 (C⁸, C⁹, C¹⁶ and C¹⁷), 125.8 (C⁶ or C¹⁹), 125.6 (C⁶ or C¹⁹), 124.8 (C¹¹ or C¹⁴), 124.7 (C¹¹ or C¹⁴), 117.2 (C²¹), 107.3 (C³), 103.8 (C⁴), 55.3 (Me).

[Ru(phen)₂(4-DEA-Sal)]BF₄ (**12**). Yield 90%. Anal. Calcd for C₃₃H₃₀BF₄N₅O₃Ru: C, 56.77; H, 4.08; N, 9.46. Found: C, 56.83; H, 4.12; N, 9.43. IR (KBr, cm⁻¹): 1611 (s, C=O), 1059 (s, B–F). ¹H NMR (400 MHz, DMSO-*d*₆): δ ppm 9.17 (m, 2H, H²⁰ and H⁵), 8.79 (td, 2H, H⁷ and H¹⁸), 8.52 (s, 1H, H¹), 8.43 (d, 2H, H¹⁰ and H¹⁵), 8.34 (dd, 2H, H⁸ and H¹⁷), 8.25 (dd, 2H, H⁹ and H¹⁶), 8.18 (dd, 1H, H⁶), 8.11 (dd, 1H, H¹⁹), 8.01 (dd, 1H, H¹² or H¹³), 7.96 (dd, 1H, H¹² or H¹³), 7.48 (m, 2H, H¹¹ and H¹⁴), 7.07 (d, 1H, H²), 6.08 (dd, 1H, H³), 5.58 (d, 1H, H⁴), 3.24 (m, 4H, –(CH₂)–), 1.00 (t, 6H, Me). ¹³C NMR (126 MHz, DMSO-*d*₆): δ ppm 188.0 (C¹), 171.9 (C²³), 162.4 (C²²), 153.8 (C¹² or C¹³), 153.2 (C¹² or C¹³), 151.0 (C⁵ or C²⁰), 150.9 (C⁵ or C²⁰), 149.7 (C²⁷ or C²⁸), 149.4 (C²⁷ or C²⁸), 148.5 (C²⁴ or C³¹), 148.0 (C²⁴ or C³¹), 139.5 (C²), 133.3 (C⁷ or C¹⁸), 133.0 (C⁷ or C¹⁸), 131.8 (C¹⁰ or C¹⁵), 131.7 (C¹⁰ or C¹⁵), 130.3, 130.2, 129.9 and 129.8 (C²⁵, C²⁶, C²⁹ and C³⁰), 127.9, 127.6, and 127.4 (C⁸, C⁹, C¹⁶ and C¹⁷), 126.9 (C⁶ or C¹⁹), 126.6 (C⁶ or C¹⁹), 125.3 (C¹¹ or C¹⁴), 125.2 (C¹¹ or C¹⁴), 123.8 (C²¹), 105.3 (C³), 104.1 (C⁴), 44.3 (CH₂), 24.0 (Me).

Single-Crystal X-ray Details. X-ray quality single-crystals for complexes **4** and **6** were obtained by slow evaporation of concentrated ethanol/acetonitrile (1:1) solution in the refrigerator after 4–5 days, while for complexes **9**, **10**, and **11** were grown by slow diffusion of diethyl ether into a concentrated solution of the sample in methanol at room temperature.

For the complexes **9**, **10**, and **11**, the single-crystal X-ray diffraction data were collected at 160(1) K on a Rigaku OD Synergy-Hypix diffractometer using the copper X-ray radiation ($\lambda = 1.54184 \text{ \AA}$) from a dual wavelength X-ray source and an Oxford Instruments Cryojet XL cooler. For the complexes **4** and **6** instead, these data were collected at 160(1) K on a Rigaku OD XtaLAB Synergy, Dualflex, Pilatus 200 K diffractometer using a single wavelength X-ray source (Cu $K\alpha$ radiation: $\lambda = 1.54184 \text{ \AA}$) from a microfocus sealed X-ray tube and an Oxford liquid-nitrogen Cryostream cooler and at 160(1) K on a Rigaku OD SuperNova/Atlas area-detector diffractometer using Cu $K\alpha$ radiation ($\lambda = 1.54184 \text{ \AA}$) from a microfocus X-ray source and an Oxford Instruments Cryojet XL cooler, respectively.

The most suitable single-crystal was selected and mounted on a flexible loop fixed on a goniometer head using polybutene oil and immediately transferred to the diffractometer. Pre-experiment, data collection, data reduction, and analytical absorption correction²⁴ were performed using the program *CrysAlisPro*²⁵ implemented in the *Olex2* software.²⁶ The structure was solved with the *SHELXT*²⁷ small

molecule structure solution program and refined with the *SHELXL2018/3* program package²⁷ by full-matrix least-squares minimization on *F*². The *PLATON*²⁸ software program was employed to verify the results of the X-ray analysis. Further information about experimental parameters and data are reported in the CIF file.

For **9** and **10**, the ions cocrystallized with molecules of solvent (methanol). In the asymmetric unit, the solvent molecule is disordered over two sets of positions with site-occupancy factors of 0.341(6) and 0.659(6) for **10** and with site-occupancy factors of 0.341(9) and 0.659(9) for **9**. For **9**, the ions cocrystallized with molecules of methanol and diethyl ether in a ratio 1/1/0.5. A solvent mask²⁹ was used in *Olex2* to account for the residual electron density ascribed to the disordered molecules of diethyl ether. Although not present in the final model, moiety formula and sum formula in the CIF include the atoms of those molecules of solvent leading to some alerts in the checkCIF report. The F atoms of the PF₆⁻ counterion in **6** are disordered over two sets of positions with site-occupancy factors of 0.304(5) and 0.695(5). The solvent molecule of ethanol is also disordered over two sets of positions, with site-occupancy factors of 0.436(11) and 0.564(11). More details concerning the crystal structures and refinements can be found in the corresponding CIF files.

Absorption and Emission Spectra. A Jasco V-750 spectrophotometer was used to obtain UV/vis the absorption spectra, while a Cary Eclipse fluorescence spectrophotometer with a high-precision quartz fluorescence cell was to record the emission spectra. To ensure accuracy, all samples were prepared using Schlenk techniques under an argon atmosphere. Furthermore, the emission spectra were initially measured by exciting at the maximum absorption wavelength of their corresponding UV/vis absorption spectra.

Theoretical Calculations. Density functional theory (DFT) and time-dependent DFT (TD-DFT) calculations were performed using Becke's three-parameter B3LYP exchange–correlation functional^{30,31} implemented ORCA 4.2.1.^{32,33} The basis sets used to define the atoms were LANL2DZ³⁴ for Ru and def2-SVP³⁵ for the other atoms. The empirical dispersion correction was taken into account using Grimme's dispersion with Becke–Johnson damping, D3BJ.^{36,37} The solvent (acetonitrile) effects were considered within the self-consistent reaction field (SCRf) theory using the solvation model SMD of Truhlar et al.³⁸ Time dependent DFT (TD-DFT)^{39–41} calculations of the lowest-lying 50 singlets and triplets were performed in the presence of the solvent for all complexes **1–12** with the minimum-energy geometry optimized for the ground state (S₀).

Electrochemical Measurements. The electrochemical measurements were conducted using portable potentiostat/galvanostat PalmSens equipment, which was controlled by the software PSTrace4 Version 4.4.2. All experiments were performed with a three-electrode cell configuration: the working electrode consisted of a glassy carbon-disc with a diameter of 3 mm; the auxiliary electrode was a platinum-wire electrode; the reference electrode was an Ag/AgCl (MF-2052 BASi) electrode (which was separated from the bulk solution by a Vycor frit). To remove oxygen from the solution, argon was bubbled for 5 min, after which a continuous positive flow of argon was maintained throughout the entire experiment. The cyclic voltammetry (CV) technique was employed to record the measurements of the ruthenium(II) complex solutions ($5 \times 10^{-4} \text{ M}$ in acetonitrile) in the presence of [nBu₄N][PF₆] (0.1 M) as the supporting electrolyte. The scan rate used for the CV measurements was 100 mV s⁻¹ in a clockwise direction. At the end of each experiment, ferrocene was added as an internal reference to calibrate the potentials with respect to the redox pair ferrocenium/ferrocene (Fc⁺/Fc) under our experimental conditions. The potential for the Fc⁺/Fc redox couple was determined to be $E_{1/2} = 0.40 \text{ V vs SCE}$.⁴²

Cell Lines and Assay Conditions. Human drug-sensitive CEM-CRCR and multidrug-resistant CEM/ADR5000 leukemia cell lines were cultured in RPMI-1640 medium supplemented with 10% fetal bovine serum and 1% penicillin/streptomycin (Invitrogen, Darmstadt, Germany). The cells were incubated in a humidified atmosphere of 5% CO₂ in air at 37 °C. The characteristics of the multidrug-resistance phenotype of CEM/ADR5000 cells were previously described.⁴³ All compounds were first dissolved in DMSO to obtain 20 mM stock

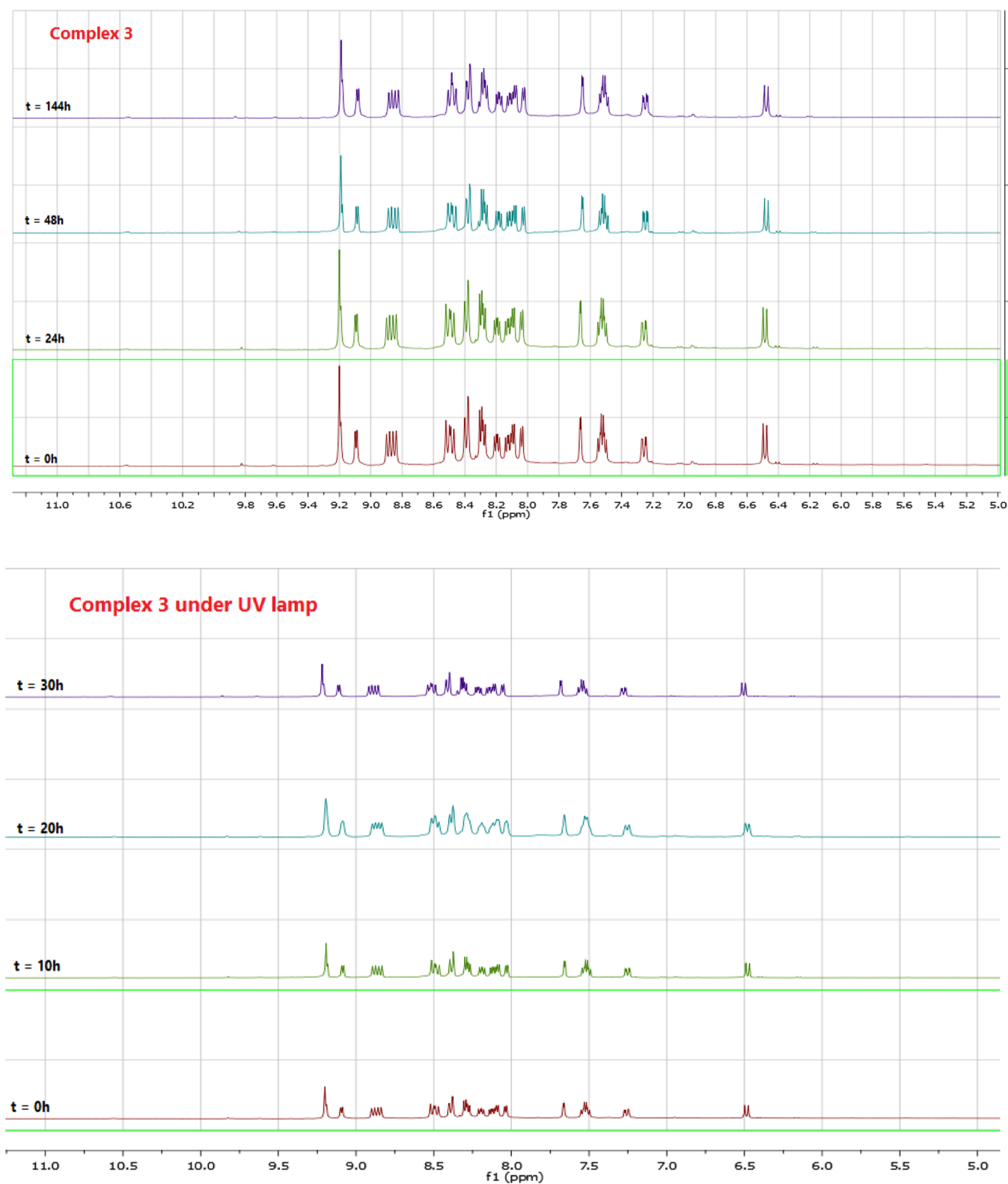


Figure 3. ^1H NMR spectra for the complex 3 in $\text{DMSO-}d_6$ (up) under environmental scattered light, (down) under UV lamp [$\lambda = 254 \text{ nm}$] at different incubation times.

solutions that were stored at -20°C and then diluted 200-folds with the assay medium before use.

Cell Proliferation Inhibition Assay. The antiproliferative activity of the 15 compounds was evaluated using the resazurin assay. CEM-CCRF cells were first exposed to the compounds at a fixed screening concentration ($10 \mu\text{M}$). To determine the IC_{50} values of the selected

most active compounds, 10 different concentrations in the range $0.3\text{--}100 \mu\text{M}$ were used for each of compound. Both CEM-CCRF and CEM/ADR5000 suspension cells were treated immediately after seeding. After 72 h incubation, $20 \mu\text{L}$ 0.01% resazurin (Promega, Mannheim, Germany) was added to each well. Resazurin fluorescence was measured after 4 h incubation using an Infinite M2000 Pro plate

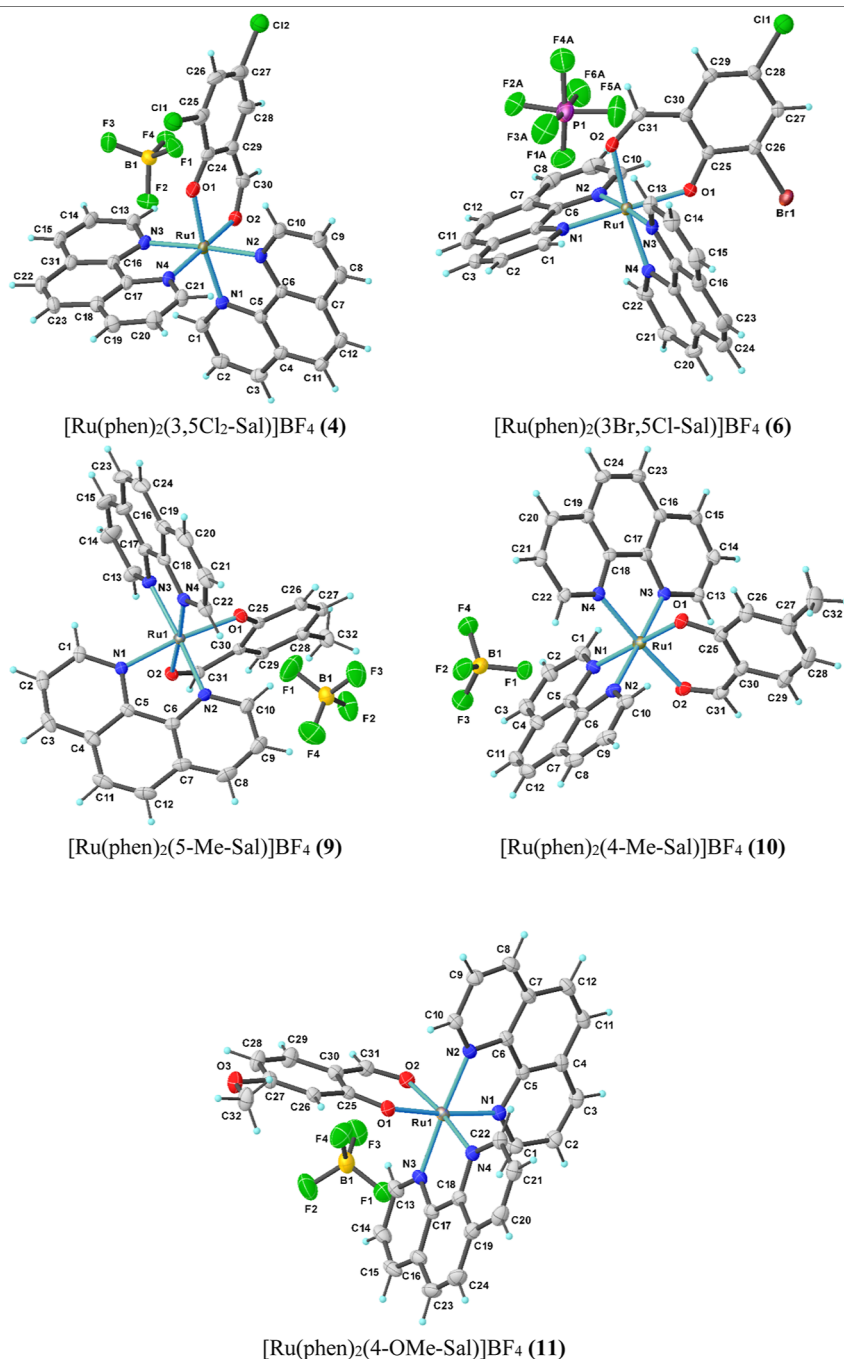


Figure 4. Molecular structure and atomic labeling scheme of 4, 6, 9, 10, and 11. Thermal ellipsoids are drawn at the 50% probability level, while the hydrogen size is arbitrary. Disordered solvent molecules have been omitted for clarity.

reader (Tecan, Crailsheim, Germany) at Ex/Em = 550 nm/590 nm wavelength.^{44,45} Cell viability was calculated in comparison to DMSO employed as the negative control. The final concentration of DMSO in the assay medium was 0.5%. The anticancer drug cisplatin was used as the positive control. This experiment was performed in triplicate with six wells each for each concentration.

Toxicity in Normal Cells. Peripheral blood was obtained from healthy donors and collected in plastic Monovette EDTA tubes, and the isolation of the mononuclear cells (i.e., human peripheral mononuclear cells “PBMC”) was accomplished using Histopaque (Sigma-Aldrich, St. Louis, MO, USA) as already reported.⁴⁶ Subsequently, 3 mL of blood was cautiously layered over 3 mL Histopaque and centrifuged at 400g for 30 min at room temperature. The PBMC-containing layer at the interface between blood serum and Histopaque was transferred into a

new tube and washed with PBS three times. The isolated cells were suspended in Panserin 413 medium (PAN-Biotech, Aidenbach, Germany) supplemented with 2.5% phytohemagglutinin M (PHA-M, Life Technologies, Darmstadt, Germany). Finally, cell viability was measured using the resazurin method as described above.

Molecular Modeling Studies. The crystal structure of DNA duplex 5′-(dCGGAAATTACCG)2–3′, cocrystallized with the inhibitor [Ru(bpy)₂dppz]²⁺ (PDB ID: 4E1U)⁴⁷ was downloaded from the protein data bank,⁴⁸ prepared by means of AutoDockTools 1.5.6,⁴⁹ and used as the DNA duplex docking target. Two docking grids were generated by means of AutoGrid 4.2.6.⁴⁹ Docking grids were centered on the experimental BP1- and BP2-bound conformations of [Ru(bpy)₂dppz]²⁺. Grid sizes were both set to 60 points on each axis (grid spacing 0.375 Å).

Table 1. Crystallographic Data for 4, 6, 9, 10, and 11

	4	6	9	10	11
empirical formula	C ₃₁ H ₁₉ BrCl ₂ F ₄ N ₄ O ₂ Ru	C ₃₃ H ₂₅ BrClF ₆ N ₄ O ₃ PRu	C ₃₃ H ₂₇ BF ₄ N ₄ O ₃ Ru	C ₃₅ H ₂₇ BF ₄ N ₄ O ₃ Ru	C ₃₅ H ₃₂ BF ₄ N ₄ O _{4.5} Ru
formula weight	738.28	886.97	715.46	715.46	768.52
temperature/K	160(1)	160(1)	160(1)	160(1)	160(1)
crystal system	triclinic	monoclinic	monoclinic	triclinic	triclinic
space group	<i>P</i> $\bar{1}$	<i>P</i> 2 ₁ / <i>n</i>	<i>P</i> 2 ₁ / <i>n</i>	<i>P</i> $\bar{1}$	<i>P</i> $\bar{1}$
<i>a</i> /Å	10.3943(3)	14.35833(10)	10.3720(1)	10.8487(2)	11.9399(2)
<i>b</i> /Å	12.1738(4)	21.06323(19)	15.5809(1)	12.13080(10)	12.6132(2)
<i>c</i> /Å	13.4918(4)	11.02611(7)	18.9897(1)	13.1787(2)	13.6491(2)
α /deg	87.818(3)	90	90	106.9530(10)	106.2550(10)
β /deg	67.579(3)	94.3527(6)	101.407(1)	107.335(2)	115.215(2)
γ /deg	66.088(3)	90	90	95.3600(10)	101.9260(10)
volume/Å ³	1428.93(8)	3325.04(4)	3008.21(4)	1552.46(4)	1654.91(5)
<i>Z</i>	2	4	4	2	2
ρ_{calc} g/cm ³	1.716	1.772	1.580	1.531	1.542
μ /mm ⁻¹	6.734	7.097	4.803	4.653	4.443
<i>F</i> (000)	736.0	1760.0	1448.0	724.0	782.0
radiation	Cu K α (λ = 1.54184)	Cu K α (λ = 1.54184)	Cu K α (λ = 1.54184)	Cu K α (λ = 1.54184)	Cu K α (λ = 1.54184)
2 θ range for data collection/deg	7.156 to 148.996	6.174 to 149.008	7.4 to 148.99	7.462 to 148.994	7.872 to 149
index ranges	-12 $\leq h \leq$ 12 -15 $\leq k \leq$ 14 -16 $\leq l \leq$ 16	-17 $\leq h \leq$ 17 -26 $\leq k \leq$ 26 -12 $\leq l \leq$ 13	-12 $\leq h \leq$ 12 -19 $\leq k \leq$ 19 -23 $\leq l \leq$ 23	-13 $\leq h \leq$ 13 -15 $\leq k \leq$ 13 -16 $\leq l \leq$ 16	-14 $\leq h \leq$ 14 -15 $\leq k \leq$ 15 -17 $\leq l \leq$ 17
reflections collected	30,162	34,292	30,950	32,154	34,392
independent reflections	5823 [<i>R</i> _{int} = 0.0470]	6791 [<i>R</i> _{int} = 0.0249]	6152 [<i>R</i> _{int} = 0.0171]	6328 [<i>R</i> _{int} = 0.0290]	6748 [<i>R</i> _{int} = 0.0203]
data/restraints/parameters	5823/0/406	6791/586/542	6152/38/439	6328/38/439	6748/0/427
goodness-of-fit on <i>F</i> ²	1.053	1.039	1.038	1.074	1.033
final <i>R</i> indexes [<i>I</i> \geq 2 σ (<i>I</i>)]	<i>R</i> ₁ = 0.0388 <i>wR</i> ₂ = 0.1052	<i>R</i> ₁ = 0.0361 <i>wR</i> ₂ = 0.1005	<i>R</i> ₁ = 0.0258 <i>wR</i> ₂ = 0.0659	<i>R</i> ₁ = 0.0349 <i>wR</i> ₂ = 0.0941	<i>R</i> ₁ = 0.0279 <i>wR</i> ₂ = 0.0761
final <i>R</i> indexes [all data]	<i>R</i> ₁ = 0.0483 <i>wR</i> ₂ = 0.1121	<i>R</i> ₁ = 0.0386 <i>wR</i> ₂ = 0.1033	<i>R</i> ₁ = 0.0270 <i>wR</i> ₂ = 0.0669	<i>R</i> ₁ = 0.0355 <i>wR</i> ₂ = 0.0945	<i>R</i> ₁ = 0.0281 <i>wR</i> ₂ = 0.0763
largest diff. peak/hole/e Å ⁻³	0.98/-0.80	1.22/-0.64	0.43/-0.75	1.15/-0.68	0.60/-0.66
CCDC number	2204680	2204679	2166691	2166690	2166692

Table 2. Selected Bond Lengths (Å) and Angles (deg) for 4, 6, 9, 10, and 11

	4		6		9		10		11	
	XRD	DFT	XRD	DFT	XRD	DFT	XRD	DFT	XRD	DFT
Ru1–N1	2.034(3)	2.076	2.038(3)	2.076	2.0357(16)	2.079	2.047(2)	2.079	2.0394(16)	2.078
Ru1–N2	2.053(3)	2.089	2.059(3)	2.088	2.0523(17)	2.090	2.051(2)	2.089	2.0573(16)	2.089
Ru1–N3	2.062(3)	2.093	2.048(3)	2.094	2.0490(17)	2.090	2.054(2)	2.090	2.0458(17)	2.090
Ru1–N4	2.032(3)	2.066	2.033(3)	2.065	2.0394(16)	2.067	2.033(2)	2.067	2.0325(17)	2.068
Ru1–O1	2.072(3)	2.085	2.051(2)	2.084	2.0526(14)	2.084	2.0548(18)	2.085	2.0643(13)	2.087
Ru1–O2	2.059(3)	2.099	2.059(2)	2.099	2.0594(13)	2.097	2.0636(18)	2.098	2.0649(14)	2.099
N1–Ru1–N2	80.17(12)	79.9	80.11(11)	79.9	80.72(6)	79.8	80.23(9)	79.8	80.20(7)	79.8
N1–Ru1–N3	98.07(12)	97.9	97.44(10)	98.2	94.82(7)	97.7	99.86(8)	97.8	96.27(7)	97.8
N1–Ru1–O1	172.66(11)	173.6	174.23(10)	173.8	173.43(6)	173.8	173.69(7)	173.8	174.17(6)	173.8
N1–Ru1–O2	85.56(11)	89.9	92.08(9)	89.9	85.07(6)	89.7	90.76(8)	89.6	88.98(6)	89.6
N2–Ru1–N3	175.88(12)	175.9	176.11(11)	176.1	173.83(7)	175.9	178.34(7)	176.0	176.23(6)	176.1
N2–Ru1–O1	92.93(11)	93.7	94.96(10)	94.0	93.57(6)	94.0	94.04(9)	94.0	93.98(6)	94.0
N2–Ru1–O2	88.82(11)	88.8	89.39(10)	88.7	89.21(6)	88.5	87.11(8)	88.5	87.82(6)	88.5
N3–Ru1–O1	88.98(11)	88.6	87.32(9)	87.9	91.11(6)	88.5	85.79(8)	88.4	89.54(6)	88.4
N3–Ru1–O2	94.77(11)	94.7	93.73(10)	94.7	94.69(6)	94.7	94.55(8)	94.7	93.47(7)	94.6
N4–Ru1–N1	91.01(12)	92.0	93.51(10)	92.4	94.90(6)	91.6	90.24(8)	91.8	94.24(6)	91.9
N4–Ru1–N2	96.05(12)	96.6	96.60(10)	96.7	95.53(7)	96.9	97.74(8)	96.9	98.47(7)	97.0
N4–Ru1–N3	80.22(12)	80.0	80.48(11)	80.0	80.52(7)	80.0	80.61(8)	79.9	80.39(7)	79.9
N4–Ru1–O1	92.24(12)	88.8	84.02(9)	88.4	88.85(6)	88.7	87.91(8)	88.6	86.28(6)	88.5
N4–Ru1–O2	173.49(11)	174.5	172.42(10)	174.4	175.19(6)	174.6	175.15(7)	174.6	173.33(6)	174.5
O1–Ru1–O2	91.82(11)	89.9	90.87(9)	89.9	91.64(5)	90.6	91.58(8)	90.6	91.11(6)	90.6

Metal complexes were built into the Maestro GUI (graphical user interface)⁵⁰ and optimized through 100 steps of B3LYP DFT

calculations using LACVP basis set for ruthenium and 6-31G* for all the other atoms.

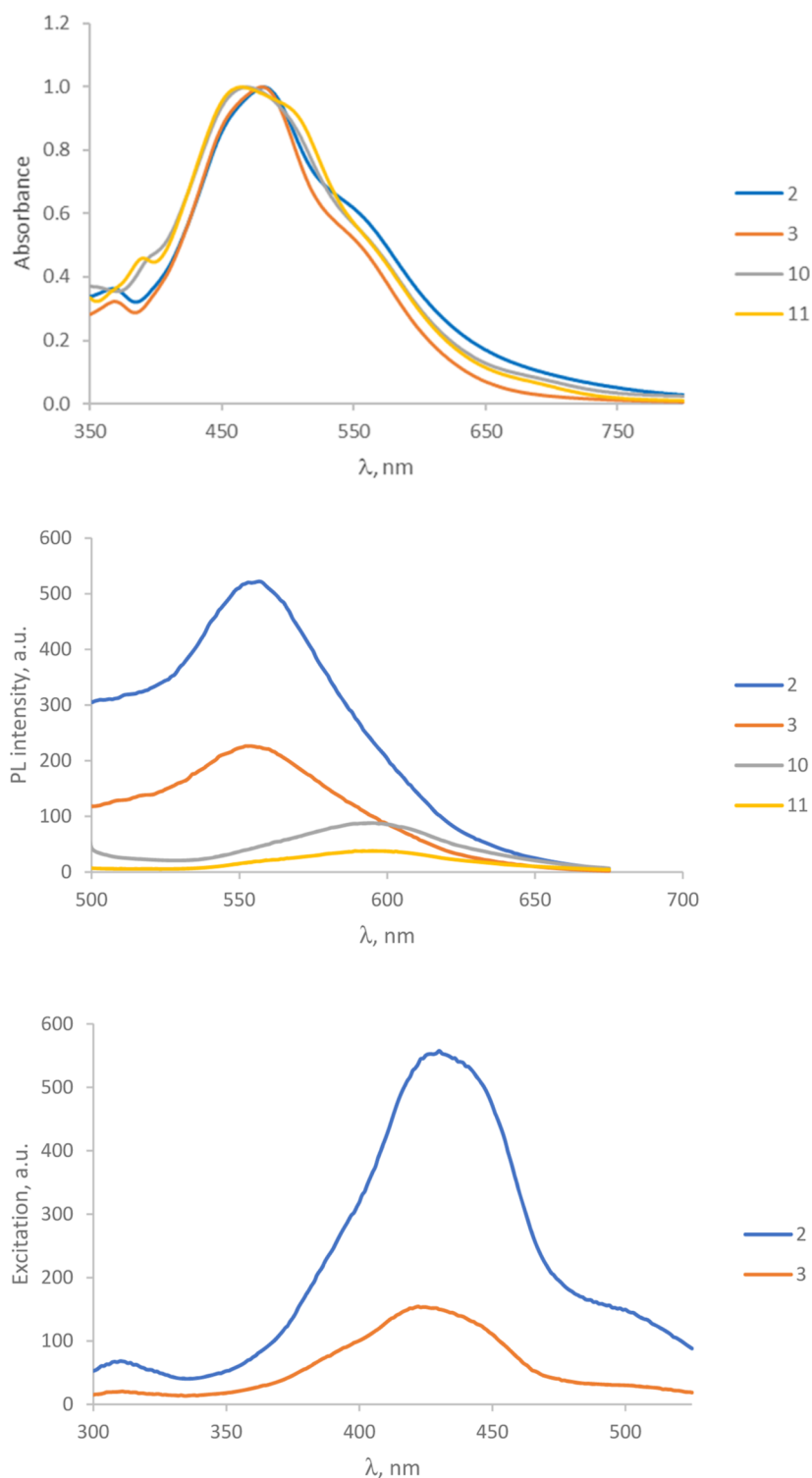


Figure 5. (Up) absorption spectra of 100 μM of all complexes in DMSO. (Middle) emission spectra of complexes (100 μM) in DMSO at $\lambda_{\text{ex}} = 475$ nm. (Down) scan of excitation spectra of complexes 2 and 3 in DMSO (100 μM) under fixed $\lambda_{\text{em}} = 555$ nm.

Docking simulations were performed using AutoDock 4.2.6.⁴⁹ Parameters for ruthenium were added to the parameters file (atom_par Pt 2.75 0.080 12.000 -0.00110 0.0 0.0 0 -1 -1 4 # Non H-bonding). For each ligand, 200 Genetic Algorithm runs were run. Population size was set to 150 individuals; the maximum number of energy evaluations was set to 2,500,000. Rates of mutation and crossover rates were set to 0.02 and 0.8, respectively. Docking poses were clustered by their atomic rmsd values using a cutoff of 2.0 Å, and the clusters were finally ranked by their lowest binding energy. The lowest energy bound

conformations for DNA-BP1/10, DNA-BP1/7, DNA-BP2/10, and DNA-BP2/7 were then submitted to MD simulations that were set up and run using Desmond,⁵¹ partial charges of 10 and 7 were retrieved from the DFT calculations. Solvation was treated explicitly using the TIP3P water model⁵² and OPLS2005 was used as the force-field.⁵³ The system was neutralized by the addition of 22 Na⁺ ions. Prior to the production stage, the four systems were relaxed using a previously reported protocol.⁵⁴ At this point, 960 ns long simulations were run in the NPT ensemble at a temperature of 310 K using a Nose–Hoover

chain thermostat and Martyna–Tobias–Klein barostat (1.01325 bar). Time steps for bonded, near, and far interactions were set to 2, 2, and 6 fs, respectively. Recording interval for MD trajectories was set to 480 ps. Except of the residues A6, T7, T18, and T19 for BP1-bound complexes, and G3, A4, A5, T20, A21, C22 for BP2-bound systems, non-H atoms were constrained by 1 kcal/mol. Atomic rmsd values of **10** and **7** over the MD trajectories were computed using the DNA structure for frames superimposition. Open source PyMOL v. 1.8.4.0 was used for visual inspection and to make molecular representations.

RESULTS AND DISCUSSION

A novel family of Ru(II) polypyridyl complexes [Ru(phen)₂(X-Sal)]BF₄ were prepared using a common procedure as reported

Table 3. Photophysical Properties for Compounds **2, **3**, **10**, and **11** Recorded in DMSO (10⁻⁵ M) at Room Temperature under Nitrogen Atmosphere with $\lambda_{\text{ex}} = 475$ nm**

compound	λ_{abs} (nm)	λ_{em} (nm)
2	478	557
3	479	554
10	471	596
11	464	595

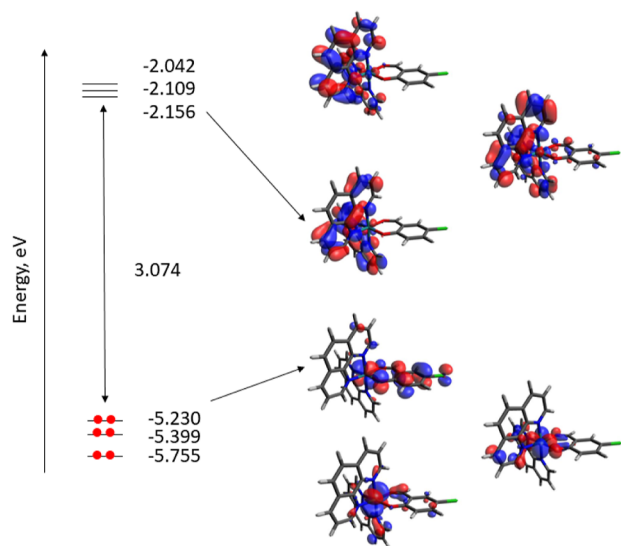


Figure 6. Energy levels and isosurface contour plots (0.03 au) for cation of compound **2**.

in the [Experimental Section](#).^{10,22,55} These complexes were characterized by elemental analysis, FT-IR, ¹H NMR, and ¹³C NMR spectroscopies, and the molecular structure of complexes **4**, **6**, **9**, **10**, and **11** was studied by X-ray diffraction analysis. Characteristic IR bands attributable to the C=O (aldehyde) and B–F (BF₄⁻) stretching frequencies and their details are provided in the [Experimental Section](#). The IR spectra exhibit a common characteristic band at ~ 1600 cm⁻¹ for $\nu(\text{C}=\text{O})$, which shifts to lower wavelength compared to free aldehyde ligands.⁵⁶ The main stretching frequency for the BF₄⁻ appears at ~ 1058 cm⁻¹.⁵⁷

The NMR spectra of all complexes are shown in [Figures S1–S12](#). In the ¹H NMR spectra, a signal for aldehyde proton (CHO) from substituted salicylaldehyde ligands is detected in the range of 8.50–9.50 ppm.⁵⁸ The aromatic protons from substituted salicylaldehyde and phen ligands appear in the range of 5.50–7.95 and 7.45–9.24 ppm, respectively. As expected, the phen ligands are nonequivalent because the nonsymmetric

nature of the salicylaldehyde ligand and the aromatic signals of the phen ligands appear as two mixed set of signals. The signals (s, 3H_{methyl}) at 2.1 ppm, (s, 3H_{methyl}) at 1.99 ppm, (s, 3H_{methoxy}) at 3.60 ppm and (m, 4H_{methine}) at 3.24 ppm, and (t, 6H_{methyl}) at 1.00 ppm are attributed to aliphatic protons for **9**, **10**, **11**, and **12** complexes, respectively. The signal at ~ 10.90 ppm assigned to phenolic proton (OH) disappears in the spectra of their complexes, indicating the deprotonation of the salicylaldehyde ligand and its coordination of oxygen atom to Ru(II) ion. In the ¹³C NMR spectra, 28 peaks in the range of 100–176 ppm are assigned to the aromatic carbon atoms and a signal at ~ 190 ppm is ascribed to the aldehyde carbon atom for all complexes. The peaks observed at 20.95, 21.42, 55.24 and 44.25, 23.97 ppm are related to the carbon atom for –CH₃ (**9**), –CH₃ (**10**), –OCH₃ (**11**), and –N(CH₂CH₃) (**12**) substituents, respectively. The existence of peaks related to aldehyde carbon and aliphatic carbon in the spectra of the complexes confirms the coordination substitution salicylaldehyde ligand to the metal ion.

Stability Studies. To check the stability of the complexes **2**, **3**, **10**, and **11**, ¹H NMR spectroscopy was used. The spectra were recorded in a quartz NMR tube at different incubation times in two modes, one under environmental scattered light and the other under UV lamp ($\lambda = 254$ nm). As shown in [Figures 3 and S13 and S14](#), their stability was confirmed in both modes as no changes in the spectra were detected over time.

X-ray Structure Analyses. The molecular structure complexes **4**, **6**, **9**, **10**, and **11** were confirmed by using the single-crystal X-ray diffraction technique. The X-ray molecular structure of these complexes with atom numbering scheme are shown in [Figure 4](#). The crystallographic data and selected bond lengths and angles are displayed in [Tables 1 and 2](#), respectively. To obtain a good crystal for structure determination, we change the counterion of complex **6** from BF₄⁻ to PF₆⁻, while this complex is used for biological assays with BF₄⁻ similar to other complexes.

All these complexes have similar structures. The compounds **4**, **10**, and **11** were crystallized in the triclinic system with and *P*1 space group and compounds **6** and **9** crystallized in the monoclinic system with the *P*2₁/*c* and *P*2₁/*n* space groups, respectively.

The crystallographic data feature that the central metal ion is six-coordinated by four nitrogen atoms of two phen ligands and the aldehyde-O and phenol-O atoms from the deprotonated aldehyde ligand, making a virtually planar five and six-membered chelate ring in the distorted octahedral geometry. This structural characteristics are perfectly consistent with what has been observed for our previous set of related polypyridyl Ru(II) complexes Δ/Λ -[Ru(bpy)₂(X,Y-Sal)]BF₄.²²

The Ru–N_{phen} bond lengths are in the range of 2.032(3)–2.062(3) Å, 2.033(3)–2.059(3) Å, 2.0357(16)–2.0523(17) Å, 2.033(2)–2.054(2) Å, and 2.0325(17)–2.0573(16) Å for complexes **4**, **6**, **9**, **10**, and **11**, respectively.

The shortest Ru–N bond lengths (Ru1–N1 and Ru1–N4, see [Table 2](#)) are those in which the pyridine ring nitrogen (N1 and N4) are trans to the oxygen atoms of substituted salicylaldehyde (O1 and O2), and this is consistent with the improved Ru(*d* π)–phen(π^*) back-bonding, which is consequent to the increase of electron density at the Ru(II) center due to the strong σ -donor effect of the deprotonated substituted salicylaldehyde ligand.

The Ru–O_{aldehyde} bond lengths are 2.059(3), 2.059(2), 2.0594(13), 2.0636(18), and 2.0649(14) Å for **4**, **6**, **9**, **10**, and

Table 4. Selected Singlet and Triplet Excited States Calculated at the TDDFT B3LYP/(def2-SVP + LANL2DZ) Level for Complex 2⁺ in DMSO Solution^a

complex	state	energy (eV)	λ (nm)	f.osc.	monoexcitations	nature	description
2	S ₁	2.200	563.6	0.0004	HOMO → LUMO (85)	$d_{\pi}(\text{Ru}) + \pi_{\text{sal}} \rightarrow \pi_{\text{phen}}^*$	¹ MLCT/ ¹ LLCT
	S ₂	2.228	556.4	0.0036	HOMO → LUMO + 1 (67)	$d_{\pi}(\text{Ru}) + \pi_{\text{sal}} \rightarrow \pi_{\text{phen}}^*$	¹ MLCT/ ¹ LLCT
	S ₃	2.252	550.6	0.0212	HOMO-1 → LUMO (70)	$d_{\pi}(\text{Ru}) \rightarrow \pi_{\text{phen}}^*$	¹ MLCT
					HOMO-1 → LUMO + 1 (15)	$d_{\pi}(\text{Ru}) \rightarrow \pi_{\text{phen}}^*$	¹ MLCT
					HOMO → LUMO + 1 (16)	$d_{\pi}(\text{Ru}) + \pi_{\text{sal}} \rightarrow \pi_{\text{phen}}^*$	¹ MLCT/ ¹ LLCT
	S ₄	2.324	533.4	0.0140	HOMO → LUMO + 2 (44)	$d_{\pi}(\text{Ru}) + \pi_{\text{sal}} \rightarrow \pi_{\text{phen}}^*$	¹ MLCT/ ¹ LLCT
					HOMO → LUMO + 3 (25)	$d_{\pi}(\text{Ru}) + \pi_{\text{sal}} \rightarrow \pi_{\text{phen}}^*$	¹ MLCT/ ¹ LLCT
					HOMO-1 → LUMO + 1 (42)	$d_{\pi}(\text{Ru}) \rightarrow \pi_{\text{phen}}^*$	¹ MLCT
	S ₅	2.338	530.4	0.0059	HOMO → LUMO + 2 (39)	$d_{\pi}(\text{Ru}) + \pi_{\text{sal}} \rightarrow \pi_{\text{phen}}^*$	¹ MLCT/ ¹ LLCT
					HOMO-2 → LUMO (49)	$d_{\pi}(\text{Ru}) \rightarrow \pi_{\text{phen}}^*$	¹ MLCT
	S ₁₁	2.717	456.4	0.1146	HOMO-1 → LUMO + 3 (15)	$d_{\pi}(\text{Ru}) \rightarrow \pi_{\text{phen}}^*$	¹ MLCT
					HOMO-2 → LUMO (17)	$d_{\pi}(\text{Ru}) \rightarrow \pi_{\text{phen}}^*$	¹ MLCT
	S ₁₃	2.930	423.2	0.1501	HOMO-2 → LUMO + 1 (29)	$d_{\pi}(\text{Ru}) \rightarrow \pi_{\text{phen}}^*$	¹ MLCT
				HOMO-2 → LUMO + 3 (19)	$d_{\pi}(\text{Ru}) \rightarrow \pi_{\text{phen}}^*$	¹ MLCT	
				HOMO-1 → LUMO + 2 (15)	$d_{\pi}(\text{Ru}) \rightarrow \pi_{\text{phen}}^*$	¹ MLCT	
				HOMO-1 → LUMO (41)	$d_{\pi}(\text{Ru}) \rightarrow \pi_{\text{phen}}^*$	³ MLCT	
				HOMO → LUMO (25)	$d_{\pi}(\text{Ru}) + \pi_{\text{sal}} \rightarrow \pi_{\text{phen}}^*$	³ MLCT/ ³ LLCT	
T ₁	1.853	669.1		HOMO → LUMO + 1 (19)	$d_{\pi}(\text{Ru}) + \pi_{\text{sal}} \rightarrow \pi_{\text{phen}}^*$	³ MLCT/ ³ LLCT	
				HOMO → LUMO (16)	$d_{\pi}(\text{Ru}) + \pi_{\text{sal}} \rightarrow \pi_{\text{phen}}^*$	³ MLCT/ ³ LLCT	
				HOMO → LUMO + 1 (49)	$d_{\pi}(\text{Ru}) + \pi_{\text{sal}} \rightarrow \pi_{\text{phen}}^*$	³ MLCT/ ³ LLCT	
T ₂	1.909	649.5		HOMO → LUMO + 1 (18)	$d_{\pi}(\text{Ru}) + \pi_{\text{sal}} \rightarrow \pi_{\text{phen}}^*$	³ MLCT	
				HOMO → LUMO + 4 (73)	$d_{\pi}(\text{Ru}) + \pi_{\text{sal}} \rightarrow \pi_{\text{sal}}^*$	³ MLCT/ ³ LC	

^aVertical excitation energies (E), dominant monoexcitations with contributions (within parentheses) of >15%, the nature of the electronic transition, and the description of the excited state are summarized.

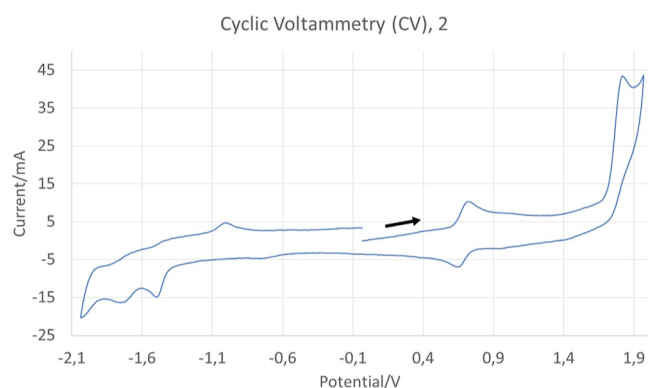


Figure 7. Cyclic voltammogram of compound 2 in acetonitrile solution (5×10^{-4} M) recorded with a scan rate of $0.10 \text{ V} \cdot \text{s}^{-1}$. The arrow indicates the starting point and the sense of the scan.

Table 5. Cyclic Voltammetry Data for Compounds 2, 3, 10, and 11 versus Fc⁺/Fc in Acetonitrile Solution (5×10^{-4} M)^a

compound	$E_{1/2}^{\text{ox}}$ (V)	$E_{1/2}^{\text{red1}}$ (V)	$E_{1/2}^{\text{red2}}$ (V)
2	+0.69 (r)	-1.50 (ir)	-1.73 (ir)
3	+0.68 (r)	-1.49 (ir)	-1.77 (ir)
10	+0.62 (r)	-1.55 (ir)	-1.79 (ir)
11	+0.61 (r)	-1.56 (qr)	-1.80 (qr)

^aMeasured using $0.1 \text{ M } [^n\text{Bu}_4\text{N}][\text{PF}_6]$ as the supporting electrolyte and a scan rate of $0.10 \text{ V} \cdot \text{s}^{-1}$ (r = reversible, qr = quasi-reversible, ir = irreversible). $E^\circ(\text{Fc}/\text{Fc}^+) = 0.400 \text{ V}$ vs SCE.

11, respectively. The Ru–O_{phenol} bond lengths are 2.072(13), 2.052(2), 2.0526(14), 2.0548(18), and 2.0643(13) Å for 4, 6, 9, 10 and 11, respectively. The Ru–N bond trans to the Ru–O_{phenol} bond (for 4: 2.034(3) Å, 6: 2.039(3) Å, 9: 2.0357(16) Å,

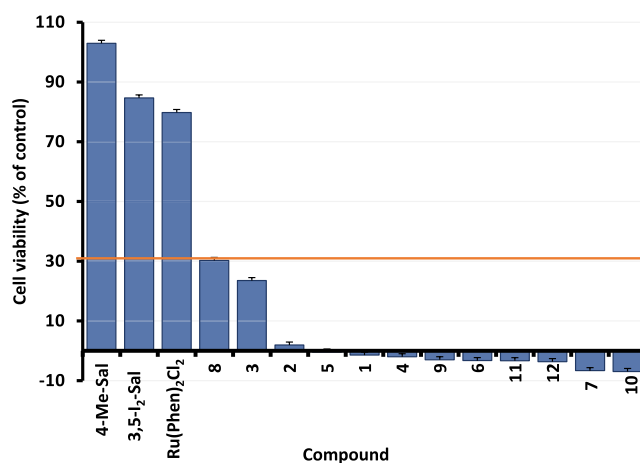


Figure 8. Cytotoxicity (depicted as % of residual cell viability) of the 15 compounds toward CCRF-CEM leukemic cells at $10 \mu\text{M}$ as measured by the resazurin reduction method. All data are presented as mean \pm SE of three independent experiments.

10: 2.047(2) Å and 11: 2.0394(16) Å) is slightly different than the Ru–N bond trans to Ru–O_{aldehyde} bond (4: 2.032(3) Å, 6: 2.033(3) Å, 9: 2.0394(16) Å, 10: 2.033(2) Å, and 11: 2.0325(17) Å.

The bite angles of the O(1)–Ru–O(2) for complexes 4, 6, 9, 10, and 11, respectively, are $91.82(11)^\circ$, $90.86(9)^\circ$, $91.64(5)^\circ$, $91.58(8)^\circ$, and $91.11(6)^\circ$, which corresponds well with the bite angle obtained of $90.26(13)^\circ$ for $[\text{Ru}(\text{bpy})_2(\text{Br-Sal})]\text{BF}_4$ and of $91.10(17)^\circ$ for $[\text{Ru}(\text{bpy})_2(\text{Cl}_2\text{-Sal})]\text{BF}_4$ in our previous work.²² The most obvious distortion of the ideal octahedral geometry results from the constrained N–Ru–N bite angles of the phen ligands, which are near 80° for all complexes (Table 2).

Table 6. Results of the Screening Assay at 10 μM against CCRF-CEM Leukemic Cells Reported as % of Residual Cell Viability

compound	cell viability % (\pm SD)
1	-1.02 ± 2.01
2	1.93 ± 1.74
3	23.51 ± 1.83
4	-0.25 ± 1.62
5	-0.40 ± 5.03
6	-0.58 ± 1.10
7	-3.11 ± 1.43
8	30.27 ± 3.03
9	-2.98 ± 1.39
10	-3.06 ± 0.96
11	-2.74 ± 1.64
12	-1.05 ± 0.40
Ru(phen) ₂ Cl ₂	79.79 ± 2.33
4-Me-Sal	97.13 ± 3.20
3,5-I ₂ -Sal	84.68 ± 5.75

It should be noted that bite angles near to 80° for phen ligands are usual for this class complex that is because of geometrical requirements of the chelate rings formed by the phen ligands.^{22,59}

Photophysical Properties. The absorption and emission spectra of compounds **2**, **3**, **10**, and **11** recorded in DMSO at room temperature as examples of all compounds are shown in Figure 5 (up). The corresponding photophysical data for these complexes are collected in Table 3. The weakest absorption bands are observed in the visible region (460–480 nm) which

Table 7. Cytotoxicity Data of 7 and 10 toward Drug-Sensitive CCRF-CEM, Multidrug-Resistant CEM/ADR5000, and Healthy PBMC Cells Determined by Resazurin Reduction Assay^a

compound	CCRF-CEM		CE-M/ADR5000		PBMC		degree of resistance
	IC ₅₀ (μM)	SD	IC ₅₀ (μM)	SD	IC ₅₀ (μM)	SD	
7	0.78	0.02	7.17	0.53	1.72	0.09	9.19
10	0.52	0.08	5.56	1	10.15	0.73	10.69
cisplatin	5.82	0.16	3.28	0.41			0.56

^aAll values are expressed as mean \pm standard deviation (SD) of three independent experiments. The degree of resistance was calculated by dividing the IC₅₀ value of resistant cells by that of sensitive cells.

are attributed to MLCT transitions.⁶⁰ Taking compound **10** as a reference, complexes **2** and **3** (with halogen in the ligand) show a bathochromic shift, while compound **11** (with methoxy-substituent) show a hypsochromic shift. Regarding the light emission, excitation of the solutions of the four compounds **2**, **3**, **10**, and **11** at 475 nm resulted in a weak visible-light emission especially for complex **11** which appears almost quenched [Figure 5 (middle)]. For compounds **2** and **3** with higher emission, the excitation spectra were scanned by fixing the λ_{em} in 550 nm to find λ_{ex} which gives us the maximum emission intensity [Figure 5 (down)]. As shown in Figure 5 (down), the λ_{ex} is about 430 nm. The values of the emission spectra are collected in Table 3 and are attributed to ³MLCT/³LLCT (see theoretical calculations). The comparison between these photophysical results (both absorption and emission) and

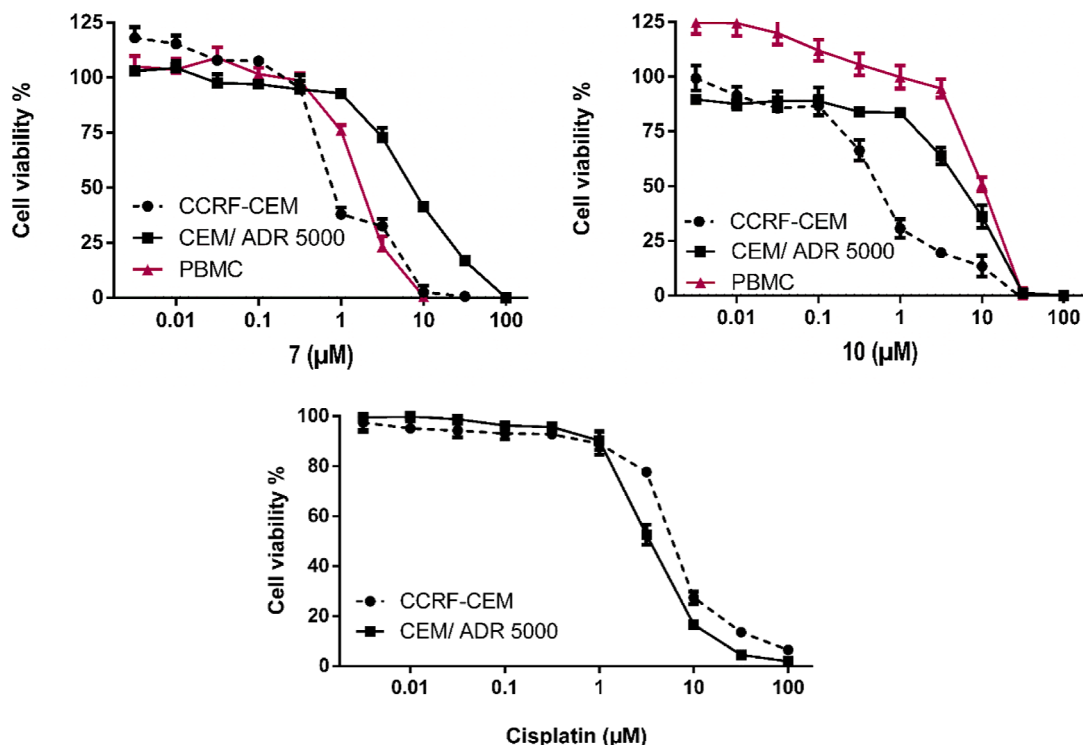


Figure 9. Cytotoxicity profile of the top two most active compounds **7** and **10** toward drug-sensitive parental CCRF-CEM tumor cells and their P-glycoprotein (MDR1/ABCB1)-expressing, multidrug-resistant subline CEM/ADR5000 as determined by resazurin reduction assays. Moreover, human peripheral mononuclear cells (PBMC) were investigated as normal counterparts to the leukemia cell lines. Cisplatin was used as a positive control to verify the multidrug resistance phenotype of the CEM/ADR5000 cells. All data are presented as mean \pm SE of three independent experiments.

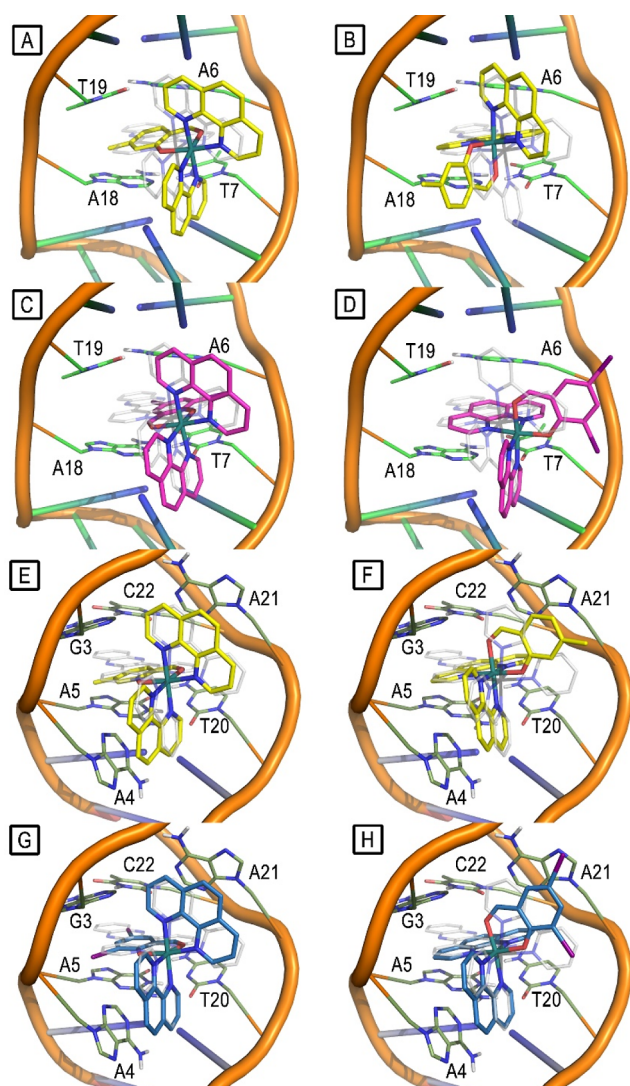


Figure 10. Salicyl-orientated (panel A) and aryl-orientated (panel B) docking poses of complex **10** (yellow sticks) bound to BP1 (green sticks). Salicyl-orientated (panel C) and aryl-orientated (panel D) docking poses of complex **7** (magenta sticks) bound to BP1 (green sticks). Salicyl-orientated (panel E) and aryl-orientated (panel F) docking poses of **10** (yellow sticks) bound to BP2 (olive sticks). Salicyl-orientated (panel G) and aryl-orientated (panel H) docking poses of complex **7** (magenta sticks) bound to BP2 (olive sticks). DNA phosphodiester backbone is represented in orange cartoons. $[\text{Ru}(\text{bpy})_2\text{dppz}]^{2+}$ experimental position is depicted for reference, in every panel, as white transparent sticks.

those of the related complexes with bipyridine ligands published by us²² reveals a hypsochromic shift in the phenanthroline derivatives. The TD-DFT calculations (see below) show that absorptions in both series of complexes are transitions from the metal to π^* -molecular orbitals of the bipyridine or phenanthroline ligands, and the energy of the transitions is higher in the case of the complexes bearing phenanthroline ligands.

Theoretical Calculations. DFT and TD-DFT calculations were carried out on the cationic of complexes (without consideration of the anion) to get a deeper understanding of their electrochemical and photophysical properties. Calculations were developed at the B3LYP/def2-SVP + LANL2DZ) level including solvent (DMSO) effects (see [Experimental Section](#) for calculation details). [Table 2](#) gathers some calculated structural

values of the computed complexes in their electronic ground states (S_0), and the comparison with the experimental XRD values showing a good agreement between bond distances, angles, and torsional angles validating the level of theory.

[Figure 6](#) displays the isovalue contour plots calculated for the frontier molecular orbitals (MOs) at the electronic ground state (S_0) of the cationic part of compound **2**. The electronic structure of complexes **1** and **3–12** is very similar to the one calculated for compound **2** (see [Figures S15–S25](#)). In all of them, the HOMO–LUMO gap is ranging between 2.97 and 3.27 eV. In compound **2** (as a representative example), the HOMO is contributed by the orbitals of the ruthenium atom (47.3%) and the salicylaldehyde ligand (42.9%), while the LUMO, LUMO + 1, and LUMO + 2 are mainly spread over the phenanthroline ligands (see [Table S1](#)) in a similar manner as it has been described for related complexes of ruthenium with bipyridine ligands and a chelating oxygen donor ligand.^{22,61–64}

The nature of the excited states was investigated using the TD-DFT approach. The low-lying singlet and triplet states with the geometries of the ground state were calculated using this approach. [Tables 4](#) and [S2–S4](#) summarize the calculated excited states. As a representative example, for compound **2**, the absorption in the experimental spectrum ([Figure 5](#) up) appeared at 478 nm is assigned to the singlet excited state S_{13} (423.2 nm) and it is a complex transition mainly composed by transitions from the HOMO – 2 to the LUMO, LUMO + 1, and LUMO + 3, and a transition HOMO – 1 \rightarrow LUMO + 2, with a calculated oscillator strength of 0.1501. This band shows a shoulder at 537 nm assigned to the singlet excited state S_{11} (456.4 nm) which is mainly a double transition HOMO – 2 \rightarrow LUMO and HOMO – 1 \rightarrow LUMO + 3 with a calculated oscillator strength of 0.1146. For both excited states, these transitions correspond to a metal-to-ligand charge transfer ($^1\text{MLCT}$) from the ruthenium center to the phenanthroline ligands. Lower energy singlet excited states displayed very low values of the oscillator strength. Similar results can be observed with compounds **3**, **10**, and **11**.

The emission spectra for complexes **2**, **3**, **10**, and **11** are shown in [Figure 5](#) (middle). The theoretical values are underestimated, especially for complexes **10** and **11**. For complex **2**, the unstructured signal at 557 nm is assigned to the calculated excited state T_1 (669.1 nm) which corresponds mainly to transitions from the HOMO – 1 and the HOMO to the LUMO and the LUMO + 1. Since the HOMO – 1 is mainly located on the ruthenium center and the HOMO is located on the salicyl ligand (while the LUMO and the LUMO + 1 are located on the phenanthroline ligands), this transition can be described as a metal-to-ligand charge transfer ($^3\text{MLCT}$) along with a ligand-to-ligand charge transfer ($^3\text{LLCT}$). Compound **3** shows a similar unstructured signal at a slightly higher energy than compound **2** (554 nm). This band can be assigned to the excited state T_1 , although the calculated energy is underestimated (667.8 nm, see [Table S2](#)). This excited state corresponds to transitions HOMO \rightarrow LUMO and LUMO + 1 \rightarrow LUMO + 2. These transitions can be described as a combination $^3\text{MLCT}/^3\text{LLCT}$. Compound **10** displays a broad band at about 596 nm that can be assigned to the excited state T_1 . As in compound **2**, this excited state corresponds to transitions HOMO – 1 \rightarrow LUMO and HOMO \rightarrow LUMO + 1 also described as $^3\text{MLCT}/^3\text{LLCT}$. Compound **11** shows a broad and weak band at 595 nm. This band can be assigned to the calculated excited state T_2 (681.0 nm, see [Table S4](#)) and corresponds to transitions HOMO \rightarrow LUMO and HOMO \rightarrow LUMO + 1 ($^3\text{MLCT}/^3\text{LLCT}$).

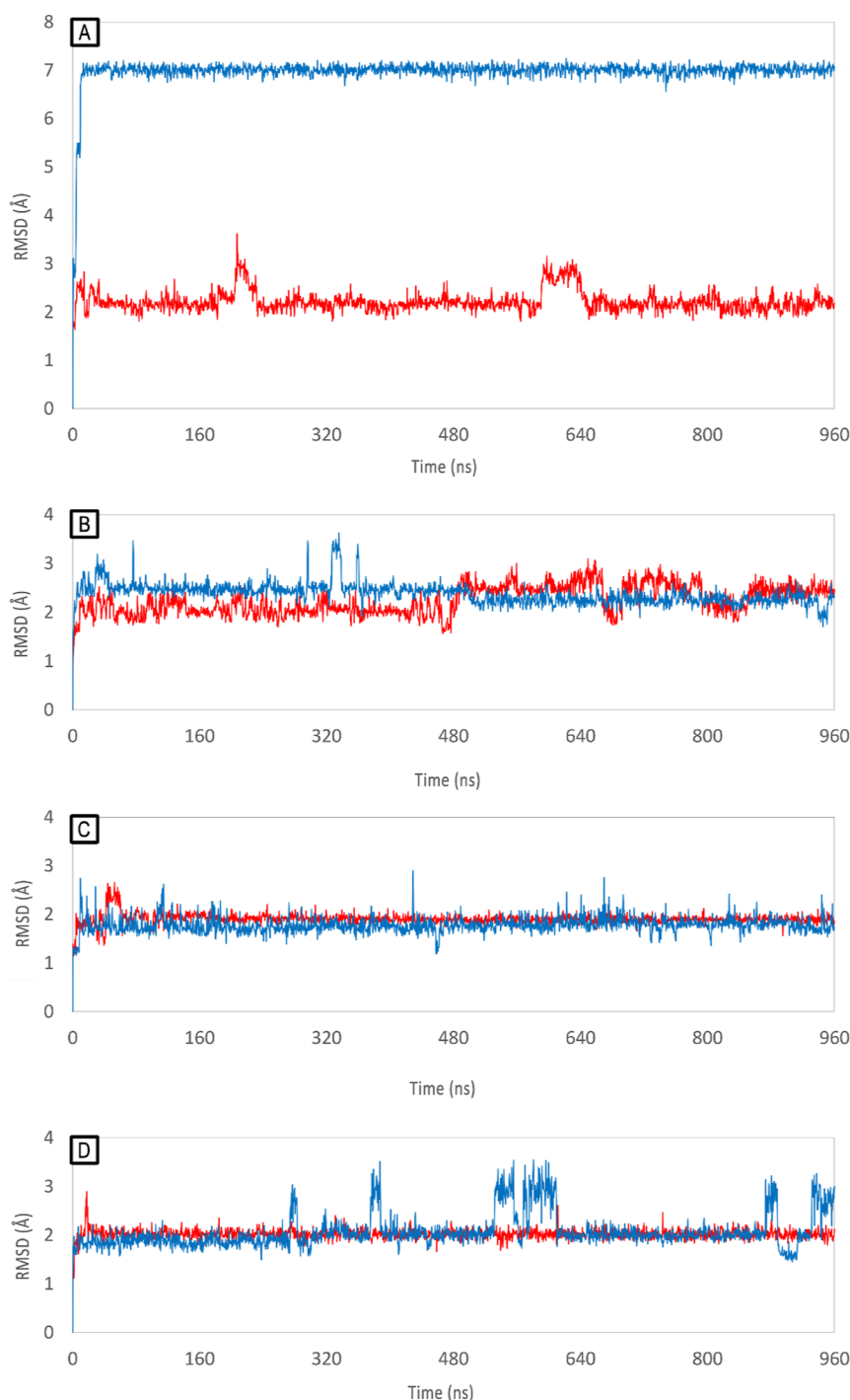


Figure 11. rmsd variations over 960 ns-long MD simulation of BP1-bound complex **10** (panel A); BP2-bound complex **10** (panel C); BP1-bound complex **7** (panel B) and BP2-bound complex **7** (panel D). Red lines represent salicyl-oriented binding mode and blue lines represent aryl-oriented binding mode.

Electrochemical Measurements. The electrochemical properties of compounds **2**, **3**, **10**, and **11** were examined by cyclic voltammetry (CV) in acetonitrile solutions (5×10^{-4} M) using $[\text{nBu}_4\text{N}][\text{PF}_6]$ (0.1 M) as the supporting electrolyte and a three-electrode setup, which incorporates a glassy carbon working electrode. The solutions were deaerated by bubbling argon. Potentials are given versus the ferrocenium/ferrocene (Fc^+/Fc) couple and the resulting cyclic voltammograms are shown in Figures 7 and S26–S28 (see data in Table 5).

The anodic region of the voltammograms features a single reversible wave of at $E_{1/2}^{\text{ox}} = 0.61\text{--}0.69$ V. It is known that for Ru(II) complexes, the first oxidation process is normally centered onto the metal.⁶⁵ For these compounds, it is reasonable to admit that the oxidation process can involve both the ruthenium center and the salicylaldehyde ligand as the HOMO is spread over this ligand and the metal. In addition, the experimental values of $E_{1/2}^{\text{ox}}$ are in good agreement with the calculated values of the energies of the HOMOs of these compounds because complexes with a more negative calculated

value of the energy of the HOMO (2 and 3) display higher values of $E_{1/2}^{\text{ox}}$. All complexes display two irreversible or quasi-reversible reduction waves that are involving the phenanthroline ligands as the LUMO is mainly centered in these chelating ligands.^{65,66} The small additional anodic peak that appears in compounds 2, 3, and 10 can be due to the formation of a new product after the irreversible reduction process. This peak does not appear in compound 11 because the reductions are quasi-irreversible and the new product is not formed.

Biological Assessments. On the basis of our ongoing research work dealing with Ru-based complexes,^{22,67} we determined to evaluate this newly synthesized panel of compounds as anticancer agents. Specifically, we employed two leukemic cell lines well established in our previous works, namely CCRF-CEM (drug-sensitive) and CEM/ADR5000 (CCRF-CEM multidrug-resistant subcell line). The compounds underwent a preliminary screening (resazurin method) at 10 μM against the drug-sensitive cell line CCRF-CEM. Two auxiliary salicylaldehyde ligands with different pattern of substitution and the starting Ru(phen)₂Cl₂ complex were selected as controls. We did not use the standard Ru-based complex NAMI-A as a positive control as our previous studies demonstrated that this compound exerts negligible cytotoxic effects against the two selected leukemic cell lines.⁶⁷ Figure 8 shows the screening results sorted by decreasing cell viability (waterfall plot). From this screening test emerged that all Ru-complexes but Ru(phen)₂Cl₂ exert an outstanding antiproliferative activity (cutoff point of 30% cell viability), highlighting the essential role of the presence of the auxiliary salicylaldehyde ligand for the biological activity. Additionally, this test evidenced the importance of the substitution pattern at this ligand as in the case of the 5-NO₂-derivative (8) and 5-Br-derivative (3) some residual cell viability (~30 and ~23%, respectively) was detected. Overall, we can state that compounds bearing a 4-EDG and 3,5-dihalogen substitution pattern at the auxiliary ligand show a superior biological activity profile as anticancer agents. No significant cytotoxic activity was detected for both auxiliary salicylaldehyde ligands. Data are summarized in Table 6.

The top two compounds, i.e., the 4-Me-derivative (10) and 3,5-I₂-derivative (7), were selected for continuous assays (IC₅₀ determination), calculation of resistance ratio, and selectivity index [SI; evaluated on human peripheral blood mononuclear cells (PBMC)]. The dose–response curves of these two top compounds and the reference drug (cisplatin) are shown in Figure 9,⁶⁸ and on the basis of these, their IC₅₀ values (Table 7) were calculated.

Both selected Ru(II) complexes displayed antiproliferative activity in the submicromolar range against CCRF-CEM cells and in the micromolar range against CEM/ADR5000 cells. Then, the IC₅₀ values have been used to calculate the degrees of resistance. Remarkably, the cross-resistance of CEM/ADR5000 to the selected two compounds was much less to that of the reference drug. Specifically, the degrees of resistance were 9.19- and 10.69-fold for 7 and 10, respectively. Interestingly, in the cytotoxicity assays performed on PBMC, these two compounds displayed IC₅₀ values higher than those measured in sensitive wild-type CCRF leukemia cells, i.e., $1.72 \pm 0.09 \mu\text{M}$ (SI = 2.2) and $10.08 \pm 0.65 \mu\text{M}$ (SI = 19.5) for 7 and 10, respectively. The 4-Me-derivative (10) displayed also higher IC₅₀ values toward PBMC as compared to multidrug-resistant CEM/ADR5000 leukemia cells ($10.08 \mu\text{M}$ vs $5.56 \mu\text{M}$), whereas the 3,5-I₂-derivative (7) revealed IC₅₀ values toward PBMC that were

between those of the two leukemic cells ($1.72 \mu\text{M}_{\text{PBMC}}$ vs $0.78 \mu\text{M}_{\text{CCRF-CEM}}$ and $7.17 \mu\text{M}_{\text{CEM/ADR5000}}$). This indicates that these two compounds may show some tumor specific inhibition (Table 7).

An approximate comparison between the biological outcomes achieved in this work with those of previous work dealing with related polypyridyl Ru(II) complexes (Δ/Λ -[Ru(bpy)₂(X,Y-Sal)]BF₄) suggests that this type of compounds may have a better applicability as anticancer agents in the treatment of hematological malignancies with respect to solid tumors as we obtained submicromolar IC₅₀ values toward the drug-sensitive strain of leukemia cells (CCRF-CEM) and SI up to 19.5 (evaluated on PBMC cells) for the [Ru(phen)₂(X-Sal)]BF₄-type complexes of the present work versus low-micromolar IC₅₀ values toward A2780 (ovarian carcinoma), A549 (lung carcinoma), and SW480 (colon adenocarcinoma) cells and SI up to 6.1 (evaluated on HeK293 cells) for the Δ/Λ -[Ru(bpy)₂(X,Y-Sal)]BF₄-type complexes of the previous work.²² With regards to the influence of the substitution pattern at the auxiliary salicyl ligand on the antiproliferative activity, a straightforward comparison between the two sets of compounds cannot be done as previous work dealt only with halogens and evidenced the trend dihalogenated > monohalogenated and Br > Cl for the Δ/Λ -[Ru(bpy)₂(X,Y-Sal)]BF₄-type complexes, whereas a more exhaustive substitution pattern was present in this work for the [Ru(phen)₂(X-Sal)]BF₄-type complexes. Previous work also indicated that these polypyridyl Ru(II) complexes are able to induce cell cycle arrest in the G0/G1 phase and apoptosis and that only those ones bearing Br as a substituent at the auxiliary ligand are related with increase of ROS levels and mitochondrial dysfunction.²² Since the new complexes are very much alike to the former ones, we determined not to repeat these assays and move forward with the molecular docking studies (see hereinafter) on the intended DNA target.

Molecular Modeling Studies. In order to investigate the cytotoxicity mechanisms exerted by our compounds, molecular modeling studies were carried out by using as a model a 12-mer oligonucleotide sequence of DNA duplex cocrystallized with the Ru-based complex [Ru(bpy)₂dppz]²⁺ (PDB: 4E1U). In this target structure, two main binding sites which can accommodate metal complexes are observed: a first binding pocket (BP1) formed by the well-matched DNA base pairs A6-T19 and T7-A18, and a binding pocket (BP2) formed by both the well-matched DNA base pairs G3-C22 and A5-T20 and the mismatched A4-A21 base pair. DNA mismatches constitute a well-known anticancer target as deficiencies in DNA mismatch repair have been associated with high rates of gene mutation and insurgence of several types of cancers.^{69,70} Compounds 10 and 7 were submitted to molecular docking simulations, and the obtained docking poses suggested that the two complexes are potentially able to interact with both BP1 and BP2, mimicking the crystallographic position of the complex [Ru(bpy)₂dppz]²⁺.⁵¹ In particular, 10 and 7 assume two main binding modes: salicyl-orientation (a) and aryl-orientation (b), for both BP1 and BP2. At BP1, in binding mode (a), the salicylaldehyde group is partially intercalated within the bases A6-T19 and T7-A18 and the two phenanthroline rings create stacking interactions with the unpaired bases A9 and A21 (Figure 10, panels A, C); in binding mode (b), one of the two phenanthroline rings is intercalated between the bases A6-T19 and T7-A18, while the second phenanthroline ring and the salicylaldehyde moiety interact with bases A9 and A21 (Figure

10, panels B, D). At BP2, in binding mode, (a) the salicylaldehyde moiety is placed between the bases G3-C22 and A5-T20 and the phenanthroline rings interact with the mismatched bases A4-A21 (Figure 10, panels E, G); in binding mode (b), one of the two phenanthroline rings is intercalated between the bases G3-C22 and A5-T20, while the second phenanthroline ring and the salicylaldehyde ring create stacking interactions with the bases A4 and A21 (Figure 10, panels F, H).

Docking-predicted poses of **10** and **7** were used as starting points for molecular dynamics simulations, in order to investigate the dynamics of the two binding modes. Comparison of the compounds RMSD variations during the simulations (Figure 11) suggests that **10** and **7** preferentially interact at BP2 (Figure 11, panels C, D) rather than to BP1 (Figure 11, panels A, B), as the rmsd values calculated for the latter one are less stable during the simulation. The simulations show that the intercalation at BP1 occurs in less a buried region compared to BP2, since the steric hindrance of the phosphodiesteric backbone and the smaller size of BP1 hamper a deep intercalation of the metal complexes through the bases. This substantially influences the interaction of aryl-oriented poses, because the shape of the aryl group is less suitable for deep intercalation than the salicylaldehyde group. Indeed, the aryl-oriented poses of both complexes remain on the lower groove of the BP1 site, stabilized by stacking with the bases A9 and A21, without penetrating between the base pairs A6-T19 and T7-A18. On the other hand, the aryl-oriented complexes are able to intercalate deeper on the BP2 site but, as evident from minor rmsd fluctuations of the salicyl-orientation (Figure 11, red lines) versus aryl-orientation (Figure 11, blue lines), the salicyl-orientation appears the most favored. Further proofs of the selectivity of salicyl-orientation toward BP2 is obtained by checking the rmsd values in Figure 11, panel A. During the simulation of the aryl-oriented pose of complex **10** on BP1 (Figure 11, panel A, blue line) the complex escapes from the site and binds to BP2 by intercalation of its salicylaldehyde moiety. Based on these studies and in accordance with biological data reported above, we can hypothesize that the higher SI of compound **10** compared to compound **7** (i.e., 19.5 vs 2.2, respectively) is due to the higher propensity of the former to intercalate DNA BP2 which contains mismatched base pairs.

CONCLUSIONS

In this work, we synthesized and characterized (elemental analysis and spectroscopic methods) a new panel of Ru(II) polypyridyl complexes, with general formula $[\text{Ru}(\text{phen})_2(\text{X-Sal})]\text{BF}_4$, which were designed as anticancer agents. Single-crystal X-ray diffraction analysis performed on five of them showed that these complexes possess a six-coordinated structure arranged around the metal center and an overall distorted octahedral geometry.

All these complexes have been theoretically studied by quantum chemical calculations. The geometries of the complexes are in good agreement with the experimental structures determined by X-ray diffraction. All complexes display a similar electronic structure, with the HOMO, HOMO - 1, and HOMO - 2 located in the ruthenium center (the HOMO displays an additional significant participation of the salicyl ligand) and the LUMO, LUMO + 1, and LUMO + 2 located over the phenanthroline ligands. The TD-DFT calculations have been used to assign the bands observed in the absorption and emission spectra. The absorption bands correspond to ¹MLCT from the ruthenium center to the

phenanthroline ligands. The emission bands correspond to ³MLCT/³LLCT because the HOMO is involved in these transitions, and this orbital is spread over the ruthenium center and the salicyl ligand.

In vitro biological assessments carried out on two leukemic cell lines, i.e., the CCRF-CEM cell line and its multidrug-resistant counterpart CEM/ADR500, highlighted that these complexes are endowed with remarkable cytotoxicity (IC₅₀ values in the submicromolar/low-micromolar range) and intriguing SI [up to 19.5 for the complex $[\text{Ru}(\text{phen})_2(4\text{-Me-Sal})]\text{BF}_4$ (**10**)] evaluated on PBMC]. The simultaneous presence of the metal ion and the salicyl auxiliary ligand turned out to be essential for the antiproliferative activity since both the ligands selected as controls and the complex lacking such auxiliary ligand, i.e., $\text{Ru}(\text{phen})_2\text{Cl}_2$, were inactive in the screening test at 10 μM. Moreover, the substitution pattern at the salicyl ligand also plays an important role on the biological outcome as the complexes bearing 4-EDG and 3,5-dihalogen substitution displayed superior antiproliferative activity. The in silico studies, consistently with what observed in the biological assessments, suggest that the salicylaldehyde moiety might drive the binding of the complexes toward duplex DNA mismatched base pairs highlighting its essential role in the anticancer activity.

ASSOCIATED CONTENT

Supporting Information

¹The Supporting Information is available free of charge at <https://pubs.acs.org/doi/10.1021/acs.inorgchem.3c03414>.

H NMR spectra of all complexes, 2D-NMR spectra of complexes **2**, **3**, **10**, and **11**, electronic structures of complexes **1** and **3–12**, cyclic voltammograms of complexes **3**, **10**, and **11**, fluorescence spectra of complexes **2**, **3**, **10**, and **11**, and data of theoretical calculations (PDF)

Accession Codes

CCDC 2166690–2166692 and 2204679–2204680 contain the supplementary crystallographic data for this paper. These data can be obtained free of charge via www.ccdc.cam.ac.uk/data_request/cif, or by emailing data_request@ccdc.cam.ac.uk, or by contacting The Cambridge Crystallographic Data Centre, 12 Union Road, Cambridge CB2 1EZ, UK; fax: +44 1223 336033.

AUTHOR INFORMATION

Corresponding Authors

Hadi Amiri Rudbari – Department of Chemistry, University of Isfahan, 81746-73441 Isfahan, Iran; orcid.org/0000-0002-3020-8596; Email: h.a.rudbari@sci.ui.ac.ir, hamiri1358@gmail.com

José V. Cuevas-Vicario – Departamento de Química, Facultad de Ciencias, Universidad de Burgos, 09001 Burgos, Spain; orcid.org/0000-0002-2421-1529; Email: jvcv@ubu.es

Nicola Micale – Department of Chemical, Biological, Pharmaceutical and Environmental Sciences, University of Messina, I-98166 Messina, Italy; Email: nmicale@unime.it

Authors

Maryam Taghizadeh Shool – Department of Chemistry, University of Isfahan, 81746-73441 Isfahan, Iran

Andrea Rodríguez-Rubio – Departamento de Química, Facultad de Ciencias, Universidad de Burgos, 09001 Burgos, Spain; orcid.org/0000-0002-1735-2016

Claudio Stagno – Department of Chemical, Biological, Pharmaceutical and Environmental Sciences, University of Messina, I-98166 Messina, Italy; orcid.org/0000-0002-7994-8253

Nunzio Iraci – Department of Chemical, Biological, Pharmaceutical and Environmental Sciences, University of Messina, I-98166 Messina, Italy; orcid.org/0000-0002-1359-8684

Thomas Efferth – Department of Pharmaceutical Biology, Institute of Pharmaceutical and Biomedical Sciences, Johannes Gutenberg University, 55128 Mainz, Germany

Ejlal A. Omer – Department of Pharmaceutical Biology, Institute of Pharmaceutical and Biomedical Sciences, Johannes Gutenberg University, 55128 Mainz, Germany

Tanja Schirmeister – Department of Medicinal Chemistry, Institute of Pharmaceutical and Biomedical Sciences, Johannes Gutenberg University, 55128 Mainz, Germany

Olivier Blacque – Department of Chemistry, University of Zurich, CH-8057 Zurich, Switzerland

Nakisa Moini – Department of Chemistry, Faculty Chemistry, Alzahra University, 1993891176 Tehran, Iran

Esmail Sheibani – Department of Chemistry, University of Isfahan, 81746-73441 Isfahan, Iran

Complete contact information is available at:

<https://pubs.acs.org/10.1021/acs.inorgchem.3c03414>

Author Contributions

All authors contributed significantly to the writing/editing of the manuscript and unanimously approved this final version of the article.

Notes

The authors declare no competing financial interest.

ACKNOWLEDGMENTS

The authors are grateful to the Research Council of the University of Isfahan (Iran) for support of this work. This work is based upon research funded by Iran national science foundation (INSF) under project no.4005765.

REFERENCES

- (1) WHO. *Cancer*, 2022. <https://www.who.int/news-room/factsheets/detail/cancer>.
- (2) Kargbo, R. B. KRAS Inhibitors and Target Engagement Technology: From Undruggable to Druggable Targets in Cancer Therapeutics. *ACS Med. Chem. Lett.* **2022**, *13*, 752–754.
- (3) Sen, S.; Won, M.; Levine, M. S.; Noh, Y.; Sedgwick, A. C.; Kim, J. S.; Sessler, J. L.; Arambula, J. F. Metal-based anticancer agents as immunogenic cell death inducers: The past, present, and future. *Chem. Soc. Rev.* **2022**, *51*, 1212–1233.
- (4) Allardyce, C. S.; Dyson, P. J. Metal-based drugs that break the rules. *Dalton Trans.* **2016**, *45*, 3201–3209.
- (5) Kelland, L. The resurgence of platinum-based cancer chemotherapy. *Nat. Rev. Cancer* **2007**, *7*, 573–584.
- (6) Rottenberg, S.; Disler, C.; Perego, P. The rediscovery of platinum-based cancer therapy. *Nat. Rev. Cancer* **2021**, *21*, 37–50.
- (7) Oun, R.; Moussa, Y. E.; Wheate, N. J. The side effects of platinum-based chemotherapy drugs: a review for chemists. *Dalton Trans.* **2018**, *47*, 6645–6653.
- (8) Ott, I.; Gust, R. Non Platinum Metal Complexes as Anti-cancer Drugs. *Arch. Pharm. Chem. Life Sci.* **2007**, *340*, 117–126.
- (9) Konkankit, C. C.; Marker, S. C.; Knopf, K. M.; Wilson, J. J. Anticancer activity of complexes of the third row transition metals, rhenium, osmium, and iridium. *Dalton Trans.* **2018**, *47*, 9934–9974.
- (10) Lenis-Rojas, O. A.; Roma-Rodrigues, C.; Fernandes, A. R.; Marques, F.; Perez-Fernandez, D.; Guerra-Varela, J.; Sanchez, L.; Vazquez-Garcia, D.; Lopez-Torres, M.; Fernandez, A.; et al. Dinuclear Ru(II) (bipy)₂ derivatives: Structural, biological, and in vivo zebrafish toxicity evaluation. *Inorg. Chem.* **2017**, *56*, 7127–7144.
- (11) Liu, J.; Lai, H.; Xiong, Z.; Chen, B.; Chen, T. Functionalization and cancer-targeting design of ruthenium complexes for precise cancer therapy. *Chem. Commun.* **2019**, *55*, 9904–9914.
- (12) Parveen, S. Recent advances in anticancer ruthenium Schiff base complexes. *Appl. Organomet. Chem.* **2020**, *34*, No. e5687.
- (13) Alessio, E.; Messori, L. NAMI-A and KP1019/1339, two iconic ruthenium anticancer drug candidates face-to-face: a case story in medicinal inorganic chemistry. *Molecules* **2019**, *24*, 1995.
- (14) Agonigi, G.; Riedel, T.; Zacchini, S.; Păunescu, E.; Pampaloni, G.; Bartalucci, N.; Dyson, P. J.; Marchetti, F. Synthesis and antiproliferative activity of new ruthenium complexes with ethacrynic-acid-modified pyridine and triphenylphosphine ligands. *Inorg. Chem.* **2015**, *54*, 6504–6512.
- (15) Li, S.; Xu, G.; Zhu, Y.; Zhao, J.; Gou, S. Bifunctional ruthenium (II) polypyridyl complexes of curcumin as potential anticancer agents. *Dalton Trans.* **2020**, *49*, 9454–9463.
- (16) Notaro, A.; Gasser, G. Monomeric and dimeric coordinatively saturated and substitutionally inert Ru (II) polypyridyl complexes as anticancer drug candidates. *Chem. Soc. Rev.* **2017**, *46*, 7317–7337.
- (17) Karges, J.; Blacque, O.; Jakubaszek, M.; Goud, B.; Goldner, P.; Gasser, G. Systematic investigation of the antiproliferative activity of a series of ruthenium terpyridine complexes. *J. Inorg. Biochem.* **2019**, *198*, 110752.
- (18) Monro, S.; Colon, K. L.; Yin, H.; Roque, J.; Konda, P.; Gujar, S.; Thummel, R. P.; Lilge, L.; Cameron, C. G.; McFarland, S. A. Transition metal complexes and photodynamic therapy from a tumor-centered approach: challenges, opportunities, and highlights from the development of TLD1433. *Chem. Rev.* **2019**, *119*, 797–828.
- (19) Smithen, D. A.; Monro, S.; Pinto, M.; Roque, J.; Diaz-Rodriguez, R. M.; Yin, H.; Cameron, C. G.; Thompson, A.; McFarland, S. A. Bis [pyrrolyl Ru (II)] triads: A new class of photosensitizers for metal-organic photodynamic therapy. *Chem. Sci.* **2020**, *11*, 12047–12069.
- (20) Notaro, A.; Jakubaszek, M.; Rotthowe, N.; Maschietto, F.; Vinck, R.; Felder, P. S.; Goud, B.; Tharaud, M.; Ciofini, L.; Bediou, F.; et al. Increasing the cytotoxicity of Ru (II) polypyridyl complexes by tuning the electronic structure of dioxo ligands. *J. Am. Chem. Soc.* **2020**, *142*, 6066–6084.
- (21) Kordestani, N.; Rudbari, H. A.; Fernandes, A. R.; Raposo, L. R.; Baptista, P. V.; Ferreira, D.; Bruno, G.; Bella, G.; Scopelliti, R.; Braun, J. D.; et al. Antiproliferative activities of diimine-based mixed ligand copper (II) complexes. *ACS Comb. Sci.* **2020**, *22*, 89–99.
- (22) Taghizadeh Shool, M.; Amiri Rudbari, H.; Gil-Antón, T.; Cuevas-Vicario, J. V.; García, B.; Busto, N.; Moini, N.; Blacque, O. The effect of halogenation of salicylaldehyde on the antiproliferative activities of {Δ/Λ-[Ru (bpy)₂ (X, Y-sal)] BF₄} complexes. *Dalton Trans.* **2022**, *51*, 7658–7672.
- (23) Lay, P. A.; Sargeson, A. M.; Taube, H.; Chou, M. H.; Creutz, C. Cis-Bis (2, 2'-Bipyridine-N, N') Complexes of Ruthenium (III)/(II) and Osmium (III)/(II). *Inorg. Synth.* **1986**, *24*, 291–299.
- (24) Clark, R.; Reid, J. The analytical calculation of absorption in multifaceted crystals. *Acta Crystallogr., Sect. A: Found. Adv.* **1995**, *51*, 887–897.
- (25) *CrysAlisPro*, Version 1.171.41.122a; Rigaku Oxford Diffraction Ltd.: Yarnton, Oxfordshire, England, 2021.
- (26) Dolomanov, O. V.; Bourhis, L. J.; Gildea, R. J.; Howard, J. A.; Puschmann, H. OLEX2: a complete structure solution, refinement and analysis program. *J. Appl. Crystallogr.* **2009**, *42*, 339–341.
- (27) Sheldrick, G. M. SHELXT-Integrated space-group and crystal-structure determination. *Acta Crystallogr., Sect. A: Found. Adv.* **2015**, *71*, 3–8.
- (28) Spek, A. L. Structure validation in chemical crystallography. *Acta Crystallogr., Sect. D: Biol. Crystallogr.* **2009**, *65*, 148–155.

- (29) Spek, A. L. PLATON SQUEEZE: a tool for the calculation of the disordered solvent contribution to the calculated structure factors. *Acta Crystallogr., Sect. C: Struct. Chem.* **2015**, *71* (1), 9–18.
- (30) Becke, A. D. Density-functional thermochemistry. III. The role of exact exchange. *J. Chem. Phys.* **1993**, *98*, 5648–5652.
- (31) Lee, C. T.; Yang, W. T.; Parr, R. G. Development of the Colle-Salvetti correlation-energy formula into a functional of the electron density. *Phys. Rev. B: Condens. Matter Mater. Phys.* **1988**, *37*, 785–789.
- (32) Neese, F. The ORCA program system. *Mol. Sci.* **2012**, *2*, 73–78.
- (33) Neese, F. Software update: the ORCA program system, version 4.0. *Mol. Sci.* **2018**, *8*, No. e1327.
- (34) Hay, P. J.; Wadt, W. Ab initio effective core potentials for molecular calculations. Potentials for the transition metal atoms Sc to Hg. *J. Chem. Phys.* **1985**, *82*, 270–283.
- (35) Weigend, F.; Ahlrichs, R. Balanced basis sets of split valence, triple zeta valence and quadruple zeta valence quality for H to Rn: Design and assessment of accuracy. *Phys. Chem. Chem. Phys.* **2005**, *7*, 3297–3305.
- (36) Grimme, S.; Ehrlich, S.; Goerigk, L. Effect of the damping function in dispersion corrected density functional theory. *J. Comput. Chem.* **2011**, *32*, 1456–1465.
- (37) Grimme, S.; Antony, J.; Ehrlich, S.; Krieg, H. A consistent and accurate *ab initio* parametrization of density functional dispersion correction (DFT-D) for the 94 elements H-Pu. *J. Chem. Phys.* **2010**, *132*, 154104.
- (38) Marenich, A. V.; Cramer, C. J.; Truhlar, D. G. Universal solvation model based on solute electron density and on a continuum model of the solvent defined by the bulk dielectric constant and atomic surface tensions. *J. Phys. Chem. B* **2009**, *113*, 6378–6396.
- (39) Casida, M. E.; Jamorski, C.; Casida, K. C.; Salahub, D. R. Molecular excitation energies to high-lying bound states from time-dependent density-functional response theory: Characterization and correction of the time-dependent local density approximation ionization threshold. *J. Chem. Phys.* **1998**, *108*, 4439–4449.
- (40) Jamorski, C.; Casida, M. E.; Salahub, D. R. Dynamic polarizabilities and excitation spectra from a molecular implementation of time-dependent density-functional response theory: N₂ as a case study. *J. Chem. Phys.* **1996**, *104*, 5134–5147.
- (41) Petersilka, M.; Gossmann, U. J.; Gross, E. K. U. Excitation energies from time-dependent density-functional theory. *Phys. Rev. Lett.* **1996**, *76*, 1212–1215.
- (42) Connelly, N. G.; Geiger, W. E. Chemical redox agents for organometallic chemistry. *Chem. Rev.* **1996**, *96*, 877–910.
- (43) Efferth, T.; Konkimalla, V. B.; Wang, Y. F.; Sauerbrey, A.; Meinhardt, S.; Zintl, F.; Mattern, J.; Volm, M. Prediction of broad spectrum resistance of tumors towards anticancer drugs. *Clin. Cancer Res.* **2008**, *14*, 2405–2412.
- (44) O'Brien, J.; Wilson, J.; Orton, T.; Pognan, F. Investigation of the Alamar Blue (resazurin) fluorescent dye for the assessment of mammalian cell cytotoxicity. *Eur. J. Biochem.* **2000**, *267*, 5421–5426.
- (45) Kuete, V.; Mbaveng, A. T.; Nono, E. C.; Simo, C. C.; Zeino, M.; Nkengfack, A. E.; Efferth, T. Cytotoxicity of seven naturally occurring phenolic compounds towards multi-factorial drug-resistant cancer cells. *Phytomedicine* **2016**, *23*, 856–863.
- (46) Saeed, M. E.; Mahmoud, N.; Sugimoto, Y.; Efferth, T.; Abdel-Aziz, H. Molecular determinants of sensitivity or resistance of cancer cells toward sanguinarine. *Front. Pharmacol.* **2018**, *9*, 136.
- (47) Song, H.; Kaiser, J. T.; Barton, J. K. Crystal structure of Δ -[Ru(bpy)₂dppz]²⁺ bound to mis-matched DNA reveals side-by-side metalloinsertion and intercalation. *Nat. Chem.* **2012**, *4* (8), 615–620.
- (48) Berman, H. M.; Westbrook, J.; Feng, Z.; Gilliland, G.; Bhat, T. The protein data bank. *Nucleic Acids Res.* **2000**, *28*, 235–242.
- (49) Morris, G. M.; Huey, R.; Lindstrom, W.; Sanner, M. F.; Belew, R. K.; Goodsell, D. S.; Olson, A. J. AutoDock4 and AutoDockTools4: Automated docking with selective receptor flexibility. *J. Comput. Chem.* **2009**, *30*, 2785–2791.
- (50) Schrödinger Release 2022–3: *Maestro*; Schrödinger, LLC: New York, NY, 2021.
- (51) Bowers, K. J.; Chow, E.; Xu, H.; Dror, R. O.; Eastwood, M. P.; Gregersen, B. A.; Klepeis, J. L.; Kolossvary, I.; Moraes, M. A.; Sacerdoti, F. D. Scalable algorithms for molecular dynamics simulations on commodity clusters. *Proceedings of the 2006 ACM/IEEE Conference on Super-computing*, 2006; p 43.
- (52) Jorgensen, W. L.; Chandrasekhar, J.; Madura, J. D.; Impey, R. W.; Klein, M. L. Comparison of simple potential functions for simulating liquid water. *J. Chem. Phys.* **1983**, *79*, 926–935.
- (53) Jorgensen, W. L.; Maxwell, D. S.; Tirado-Rives, J. Development and testing of the OPLS all-atom force field on conformational energetics and properties of organic liquids. *J. Am. Chem. Soc.* **1996**, *118*, 11225–11236.
- (54) Alhindi, T.; Zhang, Z.; Ruelens, P.; Coenen, H.; Degroote, H.; Iraci, N.; Geuten, K. Protein in-teraction evolution from promiscuity to specificity with reduced flexibility in an increasingly complex network. *Sci. Rep.* **2017**, *7*, 44948.
- (55) Rogers, C. W.; Patrick, B. O.; Rettig, S. J.; Wolf, M. O. Ligand-assisted O-dealkylation of bis (bipyridyl) ruthenium (II) phosphine-ether complexes. *J. Chem. Soc., Dalton Trans.* **2001**, 1278–1283.
- (56) Rosu, T.; Pahontu, E.; Maxim, C.; Georgescu, R.; Stanica, N.; Almajan, G. L.; Gulea, A. Synthesis, characterization and antibacterial activity of some new complexes of Cu (II), Ni (II), VO (II), Mn (II) with Schiff base derived from 4-amino-2, 3-dimethyl-1-phenyl-3-pyrazolin-5-one. *Polyhedron* **2010**, *29*, 757–766.
- (57) Park, J. G.; Aubrey, M. L.; Oktawiec, J.; Chakarawet, K.; Darago, L. E.; Grandjean, F.; Long, G. J.; Long, J. R. Charge delocalization and bulk electronic conductivity in the mixed-valence metal-organic framework Fe (1, 2, 3-triazolate)₂(BF₄)_x. *J. Am. Chem. Soc.* **2018**, *140*, 8526–8534.
- (58) Janzen, D. E.; Wang, X.; Carr, P. W.; Mann, K. R. Synthesis and characterization of three geometric isomers of ruthenium(II) (2, 2'-bipyridyl)(salicylaldehyde)₂. *Inorg. Chim. Acta* **2004**, *357*, 3317–3324.
- (59) Chen, C.; Ji, J.; Wang, C.-J.; Jia, A.-Q.; Zhang, Q.-F. Coordination modes of salicylaldehyde derivatives in the ruthenium (II) nitrosyl and bis (2, 2'-bipyridine) ruthenium (II) complexes. *J. Coord. Chem.* **2020**, *73*, 1306–1313.
- (60) Hu, P.; Wang, Y.; Zhang, Y.; Song, H.; Gao, F.; Lin, H.; Wang, Z.; Wei, L.; Yang, F. Novel mono-nuclear ruthenium(II) complexes as potent and low-toxicity antitumor agents: synthesis, characterization, biological evaluation and mechanism of action. *RSC Adv.* **2016**, *6*, 29963–29976.
- (61) Constantino, V. R. L.; Toma, H. E.; de Oliveira, L. F. C.; Rein, F. N.; Rocha, R. C.; de Oliveira Silva, D. Structure, spectroscopy and electrochemistry of the bis(2,2'-bipyridine)(salicylato)ruthenium(II) complex. *J. Chem. Soc., Dalton Trans.* **1999**, 1735–1740.
- (62) Das, A.; Scherer, T. M.; Mobin, S. M.; Kaim, W.; Lahiri, G. K. 9-Oxidophenalenone: a noninnocent β -diketonate ligand? *Inorg. Chem.* **2012**, *51*, 4390–4397.
- (63) Zeng, L.; Sirbu, D.; Waddell, P. G.; Tkachenko, N. V.; Probert, M. R.; Benniston, A. C. Hy-drogen peroxide assisted photorelease of an anthraquinone-based ligand from [Ru (2, 2'-bipyridine) 2 (9, 10-dioxo-9, 10-dihydroanthracen-1-olate)] Cl in aqueous solution. *Dalton Trans.* **2020**, *49*, 13243–13252.
- (64) Patil-Deshmukh, A. B.; Mohite, S. S.; Chavan, S. S. Ruthenium (II)-2, 2'-bipyridine/1, 10-phenanthroline complexes incorporating (E)-2-(((5-((4-methoxyphenyl) ethynyl) pyridin-2-yl) imino) methyl)-4-((4-nitro phenyl) ethynyl) phenol as a ligand. *Transition Met. Chem.* **2020**, *45*, 333–342.
- (65) Juris, A.; Balzani, V.; Barigelletti, F.; Campagna, S.; Belser, P.; von Zelewsky, A. Ru (II) polypyridine complexes: photophysics, photochemistry, electrochemistry, and chemiluminescence. *Coord. Chem. Rev.* **1988**, *84*, 85–277.
- (66) Monti, F.; Hahn, U.; Pavoni, E.; Delavaux-Nicot, B.; Nierengarten, J.-F.; Armaroli, N. Homoleptic and heteroleptic RuII complexes with extended phenanthroline-based ligands. *Polyhedron* **2014**, *82*, 122–131.
- (67) Askari, B.; Amiri Rudbari, H.; Micale, N.; Schirmeister, T.; Efferth, T.; Seo, E.-J.; Bruno, G.; Schwickert, K. Ruthenium (II) and palladium (II) homo-and heterobimetallic complexes: Synthesis,

crystal structures, theoretical calculations and biological studies. *Dalton Trans.* **2019**, *48*, 15869–15887.

(68) Di Pietro, M. L.; Stagno, C.; Efferth, T.; Omer, E. A.; D'Angelo, V.; Germanò, M. P.; Cacciola, A.; De Gaetano, F.; Iraci, N.; Micale, N. Antileukemia Activity and Mechanism of Platinum (II)-Based Metal Complexes. *Molecules* **2022**, *27*, 9000.

(69) Loeb, L. A. A mutator phenotype in cancer. *Cancer Res.* **2001**, *61*, 3230–3239.

(70) Strauss, B. S. Frameshift mutation, microsatellites and mismatch repair. *Mutat. Res., Rev. Mutat. Res.* **1999**, *437*, 195–203.